AGU PUBLICATIONS

Tectonics

RESEARCH ARTICLE
10.1002/2013TC003479

Key Points:
- We invert large sets of longitudinal river profiles. Fits to data are excellent
- Our history of uplift is consistent with independent geological calibration
- We have reconstructed the evolution of dynamic topography in Africa since 50 Ma

Correspondence to:
J. D. Paul,
jdp43@cam.ac.uk

Citation:
Paul, J. D., G. G. Roberts, and N. White (2014), The African landscape through space and time, *Tectonics*, *32*, doi:10.1002/2013TC003479.

Received 14 NOV 2013
Accepted 25 APR 2014
Accepted article online 4 MAY 2014

The African landscape through space and time

Jonathan D. Paul[1], Gareth G. Roberts[1,2], and Nicky White[1]

[1]Bullard Laboratories, Department of Earth Sciences, University of Cambridge, Cambridge, UK, [2]Now at Department of Earth Science and Engineering, Imperial College, London, UK

Abstract It is generally accepted that Cenozoic epeirogeny of the African continent is moderated by convective circulation of the mantle. Nevertheless, the spatial and temporal evolution of Africa's "basin-and-swell" physiography is not well known. Here we show how continental drainage networks can be used to place broad constraints on the pattern of uplift through space and time. First, we assemble an inventory of 710 longitudinal river profiles that includes major tributaries of the 10 largest catchments. River profiles have been jointly inverted to determine the pattern of uplift rate as a function of space and time. Our inverse model assumes that shapes of river profiles are controlled by uplift rate history and modulated by erosional processes, which can be calibrated using independent geologic evidence (e.g., marine terraces, volcanism and thermochronologic data). Our results suggest that modern African topography started to develop ~30 Myr ago when volcanic swells appeared in North and East Africa. During the last 15–20 Myr, subequatorial Africa was rapidly elevated, culminating in the appearance of three large swells that straddle southern and western coasts. Our results enable patterns of sedimentary flux at major deltas to be predicted and tested. We suggest that the evolution of drainage networks is dominated by rapid upstream advection of signals produced by a changing pattern of regional uplift. An important corollary is that, with careful independent calibration, these networks might act as useful tape recorders of otherwise inaccessible mantle processes. Finally, we note that there are substantial discrepancies between our results and published dynamic topographic predictions.

1. Introduction

The striking "basin-and-swell" physiography of Africa's landscape and the likelihood that it is maintained by deep Earth processes have long been recognized (Figure 1) [e.g., *Holmes*, 1944; *Burke*, 1996; *Gurnis et al.*, 2000]. It is now accepted that this physiography is a surficial manifestation of convective circulation within the sublithospheric mantle [e.g., *Burke and Gunnell*, 2008; *Al-Hajri et al.*, 2010]. Africa is a useful natural laboratory for studying regional epeirogeny for several reasons. First, it is surrounded by passive margins and has been mostly unaffected by regional shortening since Paleozoic times, aside from a short strip of plate convergence along the Mediterranean coast. Secondly, the African plate has moved slowly within a hot spot frame of reference since early Oligocene times [*Burke*, 1996; *De Wit*, 2003]. *Scotese et al.* [1988] proposed that the African plate has moved northward by less than 10° since chron 5 (~59 Ma). If so, mechanical coupling between vertical stresses at the base of the lithosphere and vertical motion at the surface is not complicated by horizontal translation [*Lithgow-Bertelloni and Richards*, 1998].

African hypsometry is strikingly anomalous since ~50% of its topography stands at elevations of greater than 500 m [*Bond*, 1978]. Long-wavelength elevation of subequatorial Africa comprises the most substantial contribution to this anomalous hypsometry (Figure 1a). *Nyblade and Robinson* [1994] showed that this region is surrounded by oceanic floor with anomalously shallow bathymetry, which suggests the existence of a convectively maintained "superswell" centered on the Kerguelen Plateau in the Southern Ocean. This "superswell" has a wavelength of $\sim 10^4$ km. More localized swells with wavelengths of $\sim 10^3$ km or less occur throughout Africa. These swells are clearly expressed by long-wavelength free-air gravity anomalies (Figure 1b) [*Tapley et al.*, 2005].

In North and East Africa, localized swells are usually magmatic (e.g., Hoggar, Tibesti, and Darfur) [*Sykes*, 1978; *Cox*, 1989; *Fishwick and Bastow*, 2011]. The largest one occurs in the Afar region where the presence of a hot plume is inferred [e.g., *Ebinger and Sleep*, 1998; *Furman et al.*, 2006]. In South and West Africa, three amagmatic swells straddle the continent-ocean boundary [*Burke*, 1996; *Al-Hajri et al.*, 2010].

Gravity and topography are strongly correlated across Africa [*McKenzie and Fairhead*, 1997; *Crosby et al.*, 2010]. At wavelengths of greater than 500 km, spectral analysis of topography and gravity from central

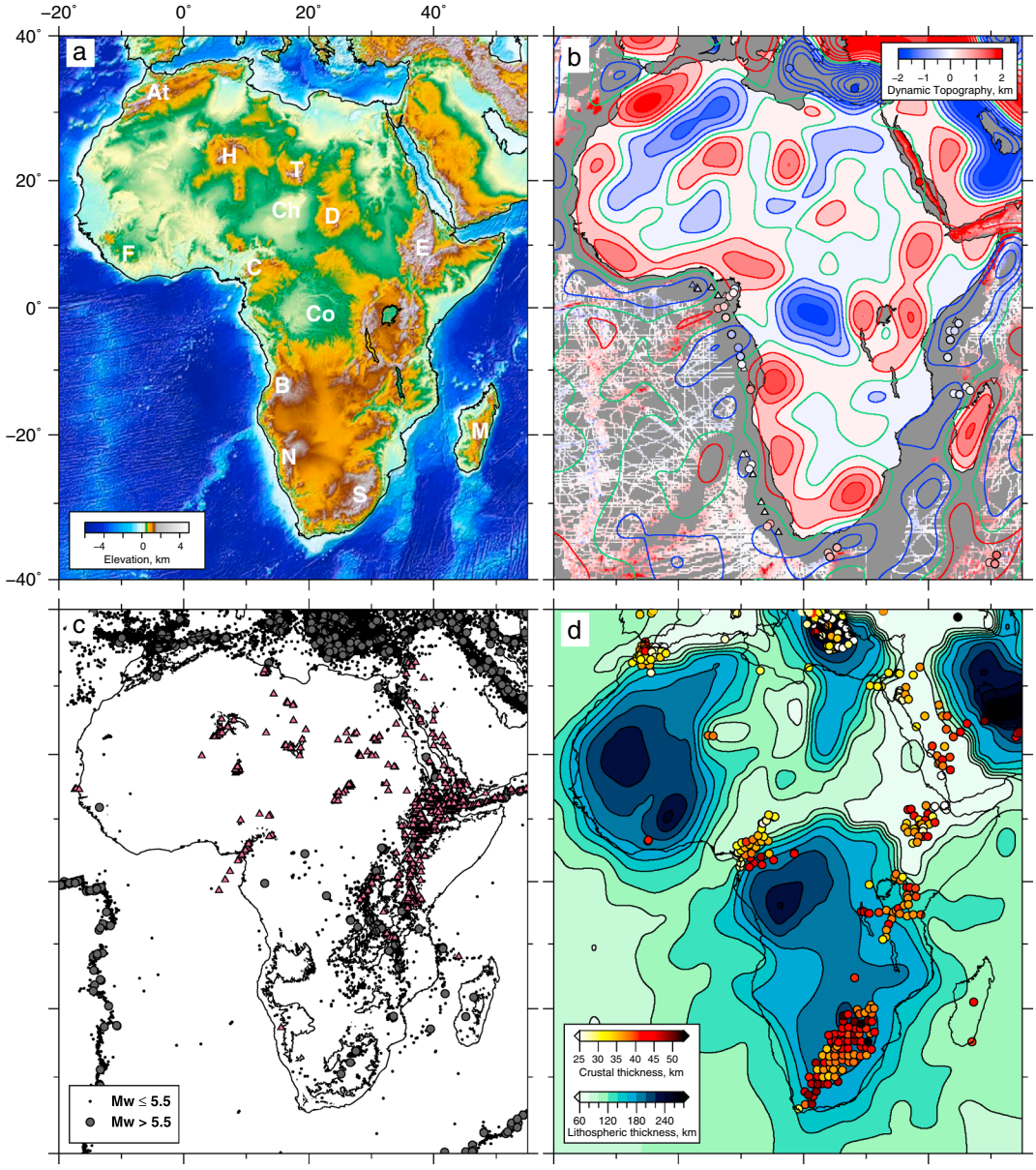

Figure 1. (a) Topographic map of Africa. At = Atlas Mountains; H = Hoggar; T = Tibesti; Ch = Chad Depression; D = Darfur; E = Ethiopian Highlands; F = Fouta Djallon; C = Cameroon Volcanic Line; Co = Congo Basin; B = Bié Dome; N = Namibian Dome; S = South African Plateau; M = Madagascar. (b) Dynamic topographic map of Africa calculated from combination of long-wavelength (800–2000 km) free-air gravity anomalies, assuming an admittance of 30 mGal km^{-1}, and residual topographic anomalies in oceanic realm [*Winterbourne et al.*, 2009]. Red, green, and blue contours = positive, zero, and negative values of dynamic topography plotted at 333 m (i.e., 10 mGal) intervals; circles = residual topographic anomalies calculated from well-constrained sedimentary and crustal thicknesses; triangles and inverted triangles = minimum and maximum estimates, respectively; sparse filigree = residual topography calculated from ship-track bathymetry and National Geophysical Data Center (NDGC) sedimentary thickness archive [*Divins*, 2008]. (c) Earthquake seismicity and volcanism. Circles = earthquakes of $M_w > 4$ between 1973 and 2013 from Incorporated Research Institutions for Seismology catalogue (www.iris.edu). Pink triangles = Cenozoic volcanism [*Thorpe and Smith*, 1974; *Woolley*, 2001; *Liégeois et al.*, 2005]. Black line = 1 km topographic contour. (d) Lithospheric thickness of Africa calculated from surface wave tomographic model [*Al-Hajri et al.*, 2010]. Contour interval = 20 km. Colored circles = estimates of crustal thickness calculated from inversion of teleseismic receiver functions [*Nair et al.*, 2006; *Dugda et al.*, 2005; *Tokam et al.*, 2010].

Africa shows that the admittance, $Z = 30–40$ mGal km^{-1} [*McKenzie and Fairhead*, 1997; *Jones et al.*, 2012]. These values imply that the Bié, Namibian, and South African swells are dynamically supported by sublithospheric density anomalies. The spatial distribution of dynamic support calculated from free-air gravity anomalies is shown in Figure 1b. Larger upwellings and downwellings are associated with minor seismicity (Figure 1c). The relationship between topography and crustal thickness variation suggests that regional uplift and subsidence are not accounted for by crustal isostasy alone (Figure 1d). Beneath elevated regions such as South Africa and the Afar region, crustal thicknesses are 33 km and 20 km, respectively [*Nair et al.*, 2006; *Dugda et al.*, 2005]. The northern margin of the Congo basin has a crustal thickness of >45 km, whereas the adjacent Cameroon Line has crustal thicknesses of 25–33 km [*Tokam et al.*, 2010].

Inferences based upon long-wavelength gravity anomalies, magmatism, and crustal thickness measurements are corroborated by the results of body wave and surface wave tomography. In the lower mantle beneath southern Africa, body wave models show that there is a large slow velocity anomaly [*Ni et al.*, 2002]. This irregularly shaped feature has a footprint of 2000 × 4000 km on the core-mantle boundary and a height of 2000 km. It is thought to be a predominantly thermal anomaly, although the sharpness of its southwestern edge suggests that compositional variation plays a moderating role [*Gurnis et al.*, 2000]. Farther north, slow shear wave velocity anomalies occur in the upper mantle beneath Afar and the Red Sea [e.g., *Gurnis et al.*, 2000; *Ritsema et al.*, 2011]. Surface wave tomographic models can be used to estimate the lithospheric thickness beneath Africa (Figure 1d) [*Priestley and McKenzie*, 2006; *Fishwick and Bastow*, 2011]. Three substantial cores of lithosphere, whose thicknesses exceed 200 km, occur in subequatorial Africa and in northwest Africa [*Priestley and McKenzie*, 2006]. These cores are associated with negative long-wavelength free-air gravity anomalies and have smaller positive anomalies distributed around their margins. Surface wave tomographic models show that slow velocity anomalies are associated with some, but not all, of these positive gravity anomalies [*Al-Hajri et al.*, 2010]. These anomalies are consistent with the presence of warm material beneath the base of the lithosphere. A thickened lithospheric keel sits beneath the Congo Basin and may coincide with convective downwelling [*Crosby et al.*, 2010].

Body wave tomographic models are often used as a basis for dynamic calculations that attempt to predict the spatial and temporal evolution of convectively maintained topography [e.g., *Lithgow-Bertelloni and Richards*, 1998; *Forte et al.*, 2010]. Some of these calculations have been tested using observed uplift rates from southern Africa [*Gurnis et al.*, 2000; *Conrad and Gurnis*, 2003]. *Moucha and Forte* [2011] simulate convective circulation backward in time from the present day to 30 Ma to predict the growth of dynamic topography. These different approaches are moderately successful in accounting for the growth of long-wavelength (>1000 km) topography. They are less successful at predicting shorter wavelength (< 1000 km) basins and swells.

The spatial and temporal organization of convective circulation that gives rise to Africa's distinctive physiography remains poorly understood. While *Ebinger and Sleep* [1998] argue that lithospheric structure exerts a fundamental control on the spatial distribution of African magmatism, *Hansen et al.* [2012] use body wave tomography to suggest that upper mantle structure is linked to deeper thermochemical upwelling. Multiple, discrete deep-seated plumes have also been invoked, based upon trace element geochemistry and joint inversion of receiver functions, gravity data, and teleseismic *S* and *SKS* arrival times [e.g., *George and Rogers*, 2002; *Chang and Van der Lee*, 2011]. Changes in lithospheric thickness and architecture probably play a key role in the generation of basaltic melt beneath Africa [*White and McKenzie*, 1995; *Priestley et al.*, 2009]. However, the spatial pattern of Cenozoic magmatism may not necessarily reflect short-wavelength dynamic support [*Jones et al.*, 2012].

Gravity- and seismology-based models do not constrain the temporal evolution of dynamic topography [e.g., *Forte et al.*, 2010]. However, stratigraphic records, especially offshore sedimentation histories, may help to constrain the development of basins and swells [*White and Lovell*, 1997; *Jones et al.*, 2012]. *Sahagian* [1988] used the elevation of Cretaceous shoreline deposits to obtain broad constraints on cumulative uplift. *Winterbourne et al.* [2009] calculated residual (i.e., dynamic) topography for the oldest oceanic lithosphere around the margins of Africa (Figure 1b). Their results show that Africa's continent-ocean boundary is warped by up to ± 1 km over wavelengths of order 10^3 km. Here we wish to investigate how onshore drainage networks respond to these changes in dynamic topography. Our principal goal is to use an inventory of longitudinal river profiles to estimate spatial and temporal patterns of dynamic topography during the Cenozoic Era.

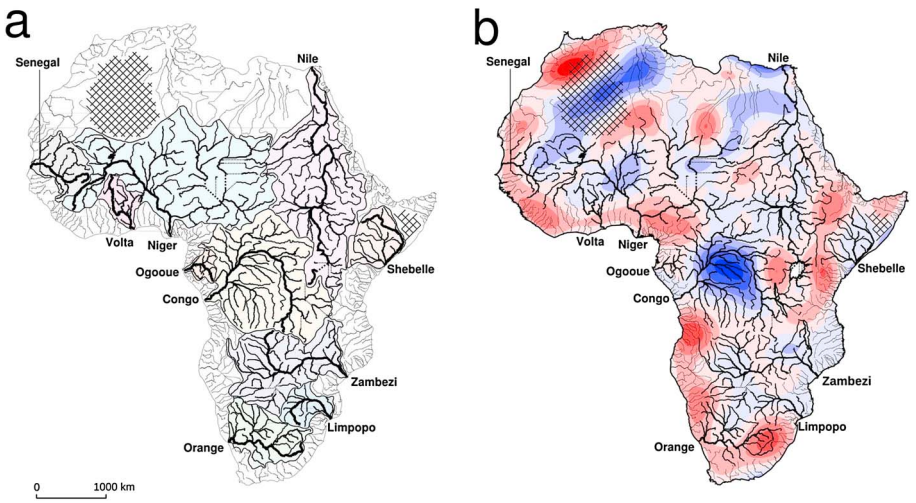

Figure 2. (a) Map of 710 rivers and 10 catchments extracted from Shuttle Radar Topography Mission (SRTM) data set. Thick lines = major rivers; intermediate lines = significant tributaries; thin lines = other rivers with Strahler order $\geq$ 5; dashed lines = interconnected lakes and/or paleodrainage. Pink, yellow, and blue shading = major catchments; coarse cross-hatching = areas without recoverable drainage. (b) Map of short-wavelength dynamic topography (Figure 1b) overlain with 710 rivers.

2. Drainage Networks and River Profiles

River profiles of 710 of Strahler order $\geq$5 were extracted from a digital topographic data set generated from the Shuttle Radar Topographic Mission [*Farr et al.*, 2007]. Flow-routing algorithms from the ArcGIS software package were used to extract the drainage network [*Tarboton*, 1997]. Sixty percent of Africa is drained by 10 large rivers and their tributaries (Figure 2). The fidelity of these calculated drainage networks was checked using Landsat imagery (Figure 3). Although drainage is sometimes absent, or masked by sand seas in arid areas (e.g., northwest Sahara Desert and Somalia), ~95% of Africa is drained by either permanent or ephemeral rivers. Drainage patterns are closely controlled by the distribution of basins and swells (Figure 2b). The majority of swells have radial drainage patterns, whereas low-lying regions are characterized by meandering drainage. This striking correlation suggests that the present-day drainage planform developed during growth of the basin-and-swell physiography.

Longitudinal profiles of 10 major African rivers are shown in Figure 4. Some of these profiles (e.g., Niger and Shebelle) are concave upward, but many others have dramatic changes of slope on different length scales (e.g., Senegal, Volta, and Zambezi). Older swells in North and East Africa, especially Hoggar and Tibesti, are drained by rivers which have mature, concave upward profiles, whereas the youthful swells of subequatorial Africa have immature, convex upward profiles.

Short-wavelength (<10 km) changes in slope (i.e., knickpoints) can be controlled by changes in bedrock lithology [e.g., *Cook et al.*, 2009]. Longer-wavelength changes in slope (i.e., knickzones) correlate poorly with lithology. Smoothly varying changes in slope are more likely to have been generated by discrete episodes of regional uplift [e.g., *Seidl and Dietrich*, 1992; *Rosenbloom and Anderson*, 1994]. Along many profiles, significant slope changes exist with wavelengths of tens to hundreds of kilometers (e.g., Senegal, Ogooue, and Limpopo rivers; Figure 4). Analysis of 710 river profiles suggests that correlations between slope or curvature and lithology are weak (Figure 5). This inference is consistent with the study of *Kirby et al.* [2003] who calculated steepness indices for channels draining eastern Tibet. They found a poor correlation between lithology and steepened reaches, which they attributed to differential rock uplift.

2.1. Inverse Modeling

Pritchard et al. [2009] and *Roberts and White* [2010] developed and applied algorithms that determine the uplift rate as a function of time, $U(t)$, required to minimize the misfit between observed and calculated river profiles. Subsequently, these approaches were generalized by *Roberts et al.* [2012a] who showed that large inventories of river profiles can be simultaneously inverted to determine uplift rate as a function of both time and space, $U(x, y, t)$. These strategies imply that uplift rate exerts the key control on the shape of a river

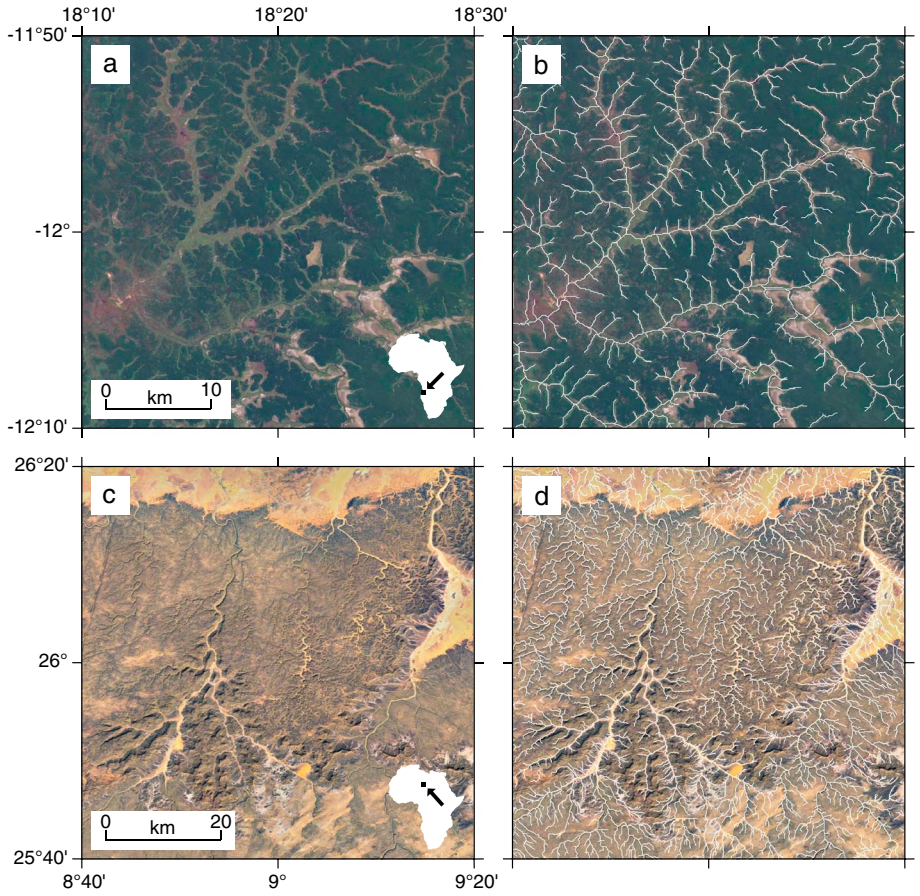

Figure 3. Fidelity of drainage patterns. (a) Landsat image (bands 2, 4, and 7) showing drainage pattern from portion of Bié Dome (see inset map). (b) Same image overlain by drainage pattern recovered from SRTM data set. (c and d) Portion of Tibesti Swell.

profile. It is thus assumed that erosive processes exercise a moderating influence [*Whipple and Tucker*, 1999; *Schoenbohn et al.*, 2004]. The shape of a river profile is governed by

$$-\frac{\partial z}{\partial t} = E(x, y, t) + U(x, y, t) \tag{1}$$

where z and x are the elevation of and the distance along a river profile, t is time before present day, and E is erosion. Knickzones are assumed to be primary manifestations of discrete uplift pulses along a profile. After a period of high uplift rate, a river profile will evolve through time as a result of headward propagation of a knickzone. In this way, a wave of erosion travels upstream, which results in localized steepening of the channel [*Whipple and Tucker*, 1999]. It is often assumed that the rate of erosion varies as a function of upstream drainage area, $A(x)$, and time, t, so that, along a river,

$$E = -vA(x)^m \left(\frac{\partial z}{\partial x}\right)^n + \kappa \frac{\partial^2 z}{\partial x^2} \tag{2}$$

where m/n is known as the concavity index [*Whipple and Tucker*, 1999]. A^m is a crude proxy for the average discharge along each river [see *Hack*, 1957; *Rosenbloom and Anderson*, 1994; *Roberts et al.*, 2012a]. If $n = 1$ and $m = 0$, v is defined as the advective (i.e., knickzone retreat) velocity. The rate at which knickzones retreat depends upon stream power, bedrock strength, and sedimentary flux [e.g., *Sklar and Dietrich*, 2001; *Brocard and van der Beek*, 2006].

In a forward model, the shape of a river profile is calculated from a given temporal and spatial distribution of uplift rate. In the absence of erosion, the shape of a river profile is simply $\int_0^t U(x, y, t)\mathrm{d}t$. The geologically more interesting inverse problem determines the smoothest uplift rate history required to fit an observed river profile. The general inverse problem is nonlinear and is solved using an optimization algorithm [*Roberts*

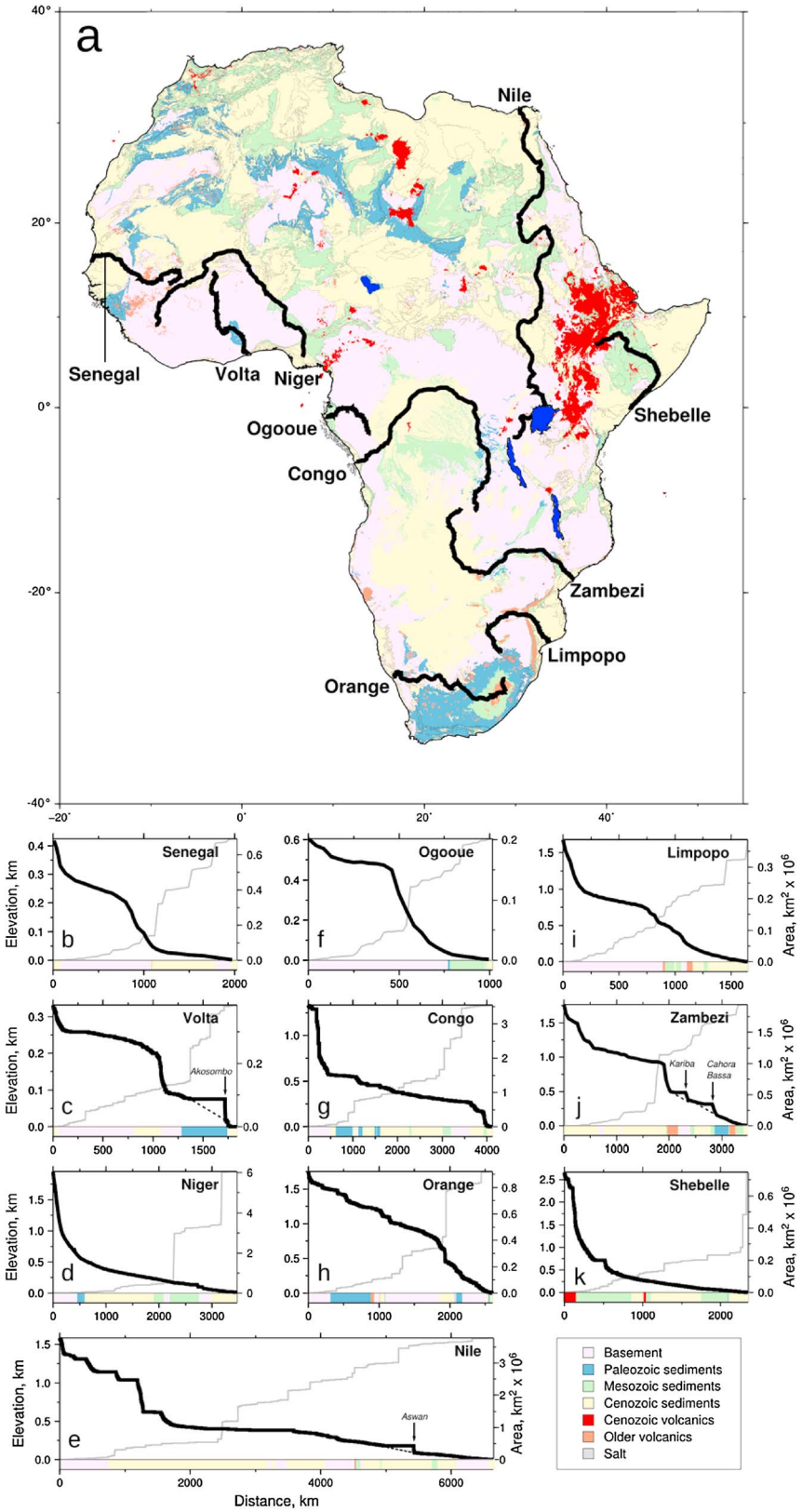

Figure 4. (a) Schematic geologic map of Africa with key at bottom right-hand side [redrawn from *Choubert and Faure-Muret*, 1976]. Thick black lines = 10 major rivers. (b–k) Longitudinal profiles of 10 major rivers. In each case, labeled arrows = major dams; dashed lines = dam-corrected profile; gray line = upstream drainage area extracted from SRTM data set; colored bar = bedrock geology along longitudinal profile. Note variable scales.

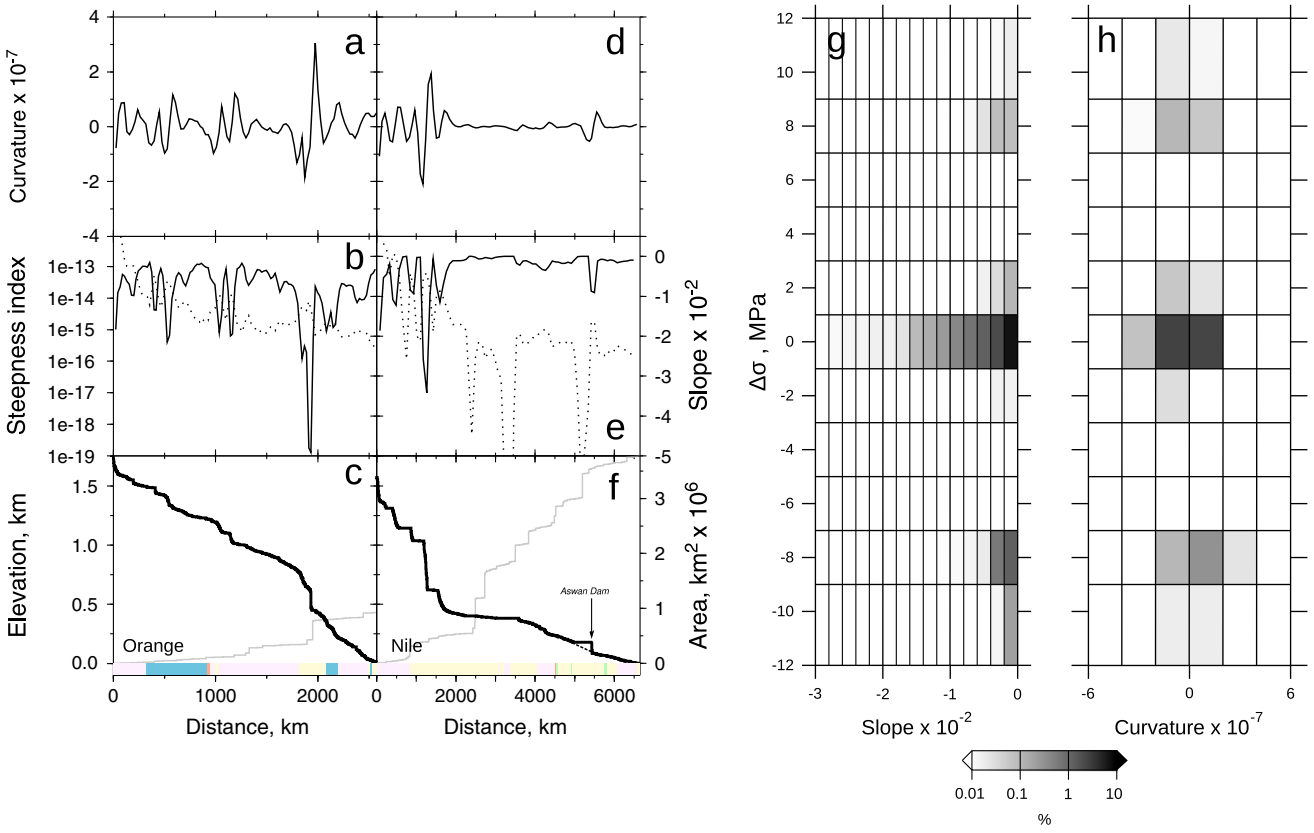

Figure 5. Relationship between longitudinal river profiles and channel geology (see Figure 4 for key). Tensile strength values based upon different lithologies reported by *Sklar and Dietrich* [2001]. (a) Channel curvature of Orange River. (b) Black line = channel slope of Orange River; dotted line = steepness index (i.e., slope divided by upstream drainage area). (c) Black line = longitudinal profile; gray line = upstream drainage area; colored bar = bedrock geology. (d–f) Nile River. (g and h) Difference in tensile strength, $\Delta\sigma_t$, as function of slope and curvature for 710 African rivers [*Sklar and Dietrich*, 2001]. In each case, maximum value of $\Delta\sigma_t$ is estimated within 5 km moving window.

et al., 2012a]. This algorithm jointly inverts large sets of river profiles by varying uplift rate through time and space. A conjugate gradient method is used to systematically vary discretized values of uplift rate until the misfit between observed and calculated river profiles is minimized [*Press et al.*, 1992]. It is important that uplift histories retrieved in this way are carefully calibrated against independent geologic observations. In this way, smooth temporal and spatial histories of uplift rate are retrieved.

2.2. Landscape Response Time

It is instructive to examine how a knickzone produced by block uplift propagates upstream with time from the mouth of a river [*Roberts et al.*, 2012a]. If $n = 1$, the time taken for a kinematic wave of incision to travel up to a given point along the river channel, τ_G, the Gilbert time, is given by

$$\tau_G = \int_{\circ}^{x} \frac{dx}{vA(x)^m} \approx \sum_{i=1}^{x} \frac{\Delta x_i}{vA(x)_i^m}, \tag{3}$$

where x is distance along the river. *Whipple* [2001] used a similar approach to derive channel response times for Taiwan by calculating v from river steepness indices and independent estimates of uplift rate. Thus, river channels act as "tape recorders" of uplift rate histories, and τ_G provides a useful estimate of the maximum recording duration. Figure 6 shows how τ_G varies across Africa. Shorter rivers along the coastline can only constrain young (i.e., Neogene) uplift events. Longer rivers that drain the continental interior potentially record older, pre-Cenozoic, events. Toward the source of the river, propagating knickzones dramatically slow down since $\tau_G \rightarrow \infty$ as $A \rightarrow 0$. Thus, drainage divides are singularities where the speed of propagating knickzones approaches zero, where the morphodynamic Péclet number becomes very small, and where diffusive and other processes dominate. Apparent juxtaposition of markedly different values of τ_G at some drainage divides in Figures 6 and 7 is a plotting artifact which has no physical meaning since $\tau_G \rightarrow \infty$ as a drainage divide is approached.

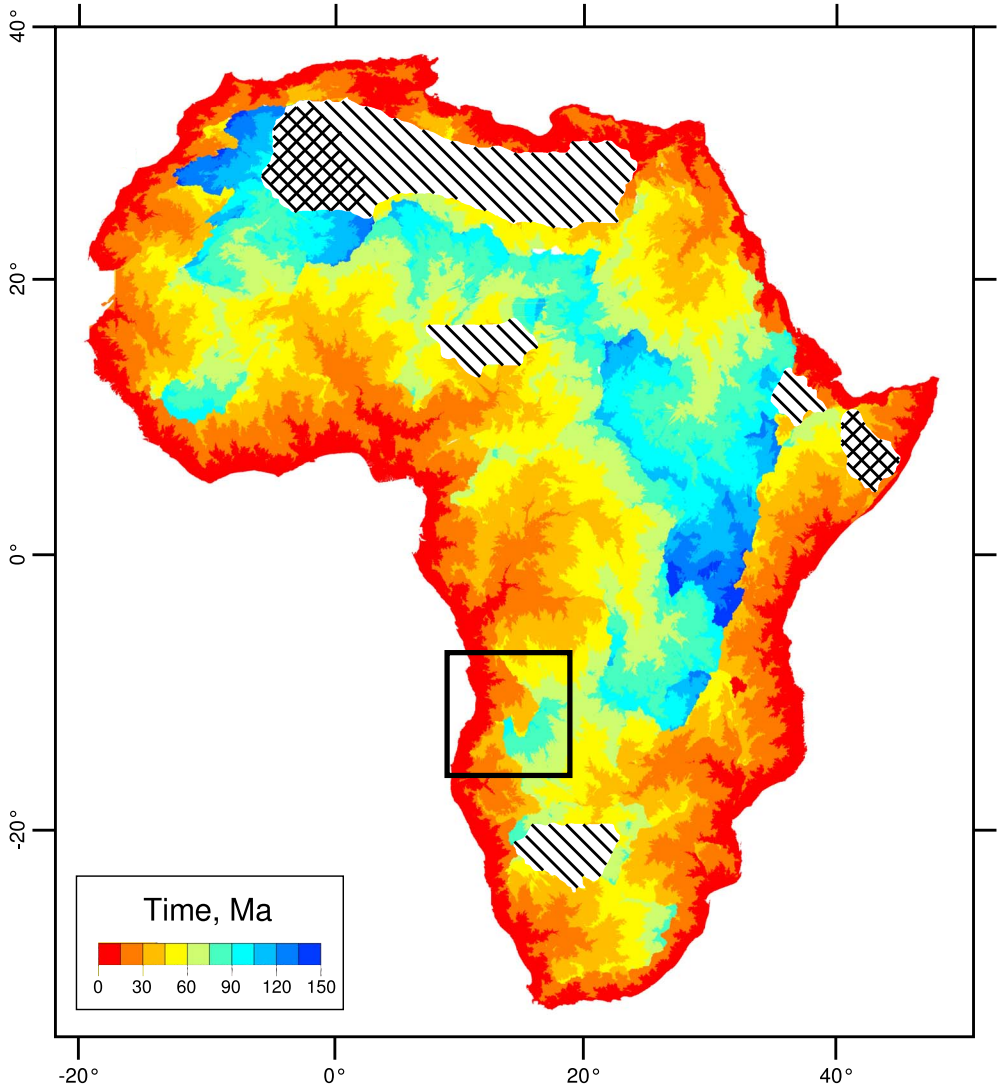

Figure 6. Landscape response time, τ_G, calculated for drainage network using equation (3). Box = location of Figure 7. Hatching and cross-hatching = regions where τ_G calculation breaks down and regions where drainage cannot be reliably recovered.

2.3. Uplift as Function of Time

The Bié dome is a high-relief topographic swell that coincides with a +30 mGal long-wavelength free-air gravity anomaly (Figures 1b and 7a). It is underlain by a patch of slow shear wave velocity at 80–100 km depth [*Fishwick and Bastow*, 2011]. Diamond-bearing kimberlites occur around the periphery of the nearby Congo Craton, suggesting that previously thickened lithosphere has subsequently been thinned [*McKenzie and Priestley*, 2008]. This swell is characterized by a radial drainage pattern and, since it intersects the coastline, westward draining rivers reach the sea over short distances. Along the coastline and shelf, there is evidence for post-Neogene uplift. Onshore, emergent Plio-Pleistocene marine terraces suggest an uplift rate of ~0.3 mm yr^{-1} which dies out further north [*Guiraud et al.*, 2010]. Offshore, the geometry and acoustic velocities of truncated deltaic foreset deposits have been used to infer >500 m of post-Pliocene uplift [*Lavier et al.*, 2001; *Jackson et al.*, 2005; *Al-Hajri et al.*, 2010].

The M'Brige, Ngunza, and Coroca Rivers drain westward across the northern, central, and southern parts of the Bié dome's western flank (Figure 7). The Ngunza River crosses directly through the center of a positive free-air gravity anomaly located over the Bié dome. Its longitudinal profile is characterized by a steep knickzone ~100 km from the coast (Figure 8d). Farther south, the Coroca River has a broader knickzone

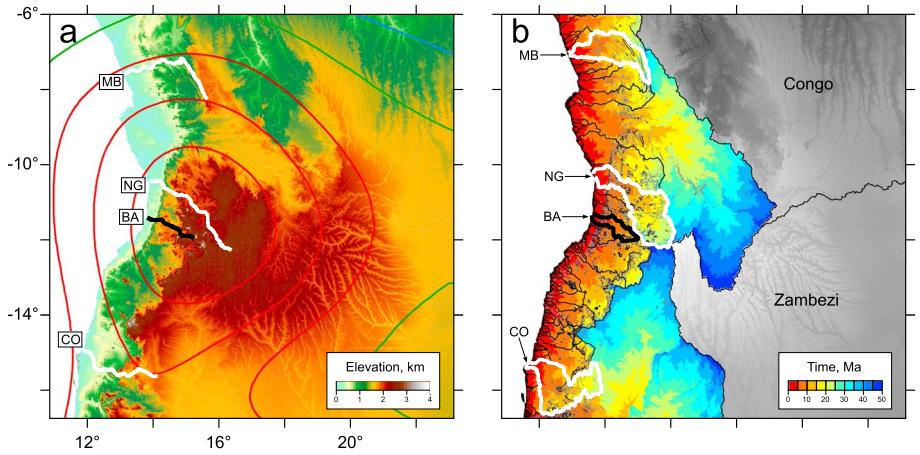

Figure 7. (a) Topographic map of Bié Dome, Angola. Colored lines = long-wavelength free-air gravity anomalies contoured every 10 mGal (red, green, and blue = positive, zero, and negative values, respectively); labeled white lines = rivers modeled in Figure 8 (MB = M'Brige; NG = Ngunza; CO = Coroca); labeled black line = Barroso River modeled in Figure 9. (b) Landscape response time, τ_G, with contour interval of 5 Myr. Gray shading = 5–15° slopes; black shading = > 15° slopes; black lines = loci of drainage divides; white/black polygons = catchments of M'Brige, Ngunza, Coroca, and Barroso Rivers.

positioned farther from the coastline (Figure 8g). Approximately 400 km north of the Bié dome, a steep knickzone occurs 400 km upstream of the mouth of the M'Brige River (Figure 8a).

These three westward draining rivers are short compared to the length scale over which swell uplift occurs, and it is reasonable to invert them by allowing uplift rate to vary as a function of time only (Figure 8). In all three cases, τ_G is small so that these profiles can only act as Neogene tape recorders.

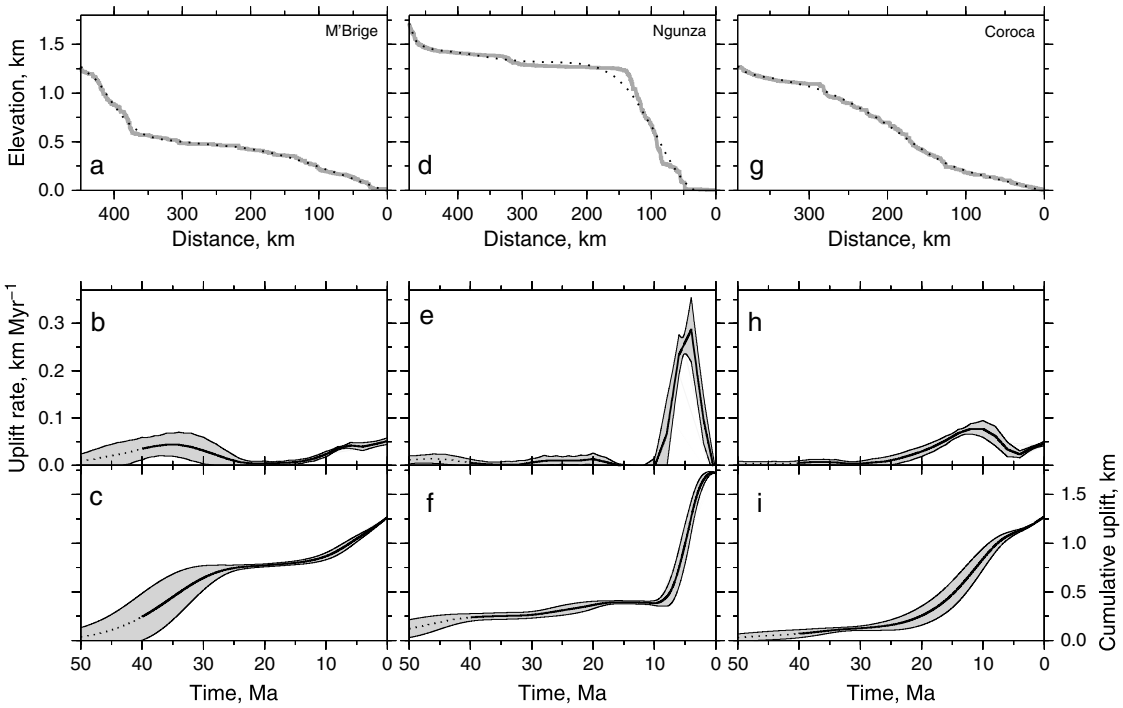

Figure 8. Inverse modeling of river profiles. Each river profile was inverted 50 times with erosion parameters assigned random values within bounded ranges ($2 \times 10^2 \le \kappa \le 7 \times 10^2$, $3.62 \le v \le 4.62$, $0.35 \le m \le 0.37$, $1 \le n \le 1.05$). (a) M'Brige River (Figure 7). Gray line = observed river profile; black dots = calculated river profile. (b) Recovered uplift rate history used to determine calculated river profile. Black line = mean uplift rate history; dotted line = unreliable uplift rate history due to breakdown of one-dimensional assumption; gray band = 1σ uncertainty obtained by *Monte Carlo* inversion. (c) Cumulative uplift (i.e., $\int_o^t U dt$). (d–f) Ngunza River. (g–i) Coroca River.

In each case, uplift rate is varied until the misfit between the calculated and observed river profile is minimized. The algorithm is highly damped, which ensures that a smooth variation of uplift rate as a function of time is obtained. *Monte Carlo* modeling helps to assess how uncertainties in the four erosional parameters (v, m, n, and κ) affect uplift rate histories. It is clear that resolution decreases with time. *Rosenbloom and Anderson* [1994] suggested that κ is probably less than 5×10^5 m^2 Ma^{-1}. Nevertheless, it is possible that κ varies by many orders of magnitude (e.g., 1–10^7 m^2 Ma^{-1}). In our case, river profiles are sampled every 10–20 km, which indicates that the minimum resolvable value of κ is 10^7 m^2 Ma^{-1}. This value exceeds all reported estimates which suggests that "erosional diffusivity" can be ignored [*Roberts et al.*, 2012a]. Advective retreat of uplift signals appears to be the dominant process.

If κ is zero, the relationship between v and m for a portion of a river profile, which was uplifted at some earlier time, is given by

$$v = \frac{\partial z}{\partial t}\left[A^m\left(\frac{\partial z}{\partial x}\right)^n\right]^{-1}. \quad (4)$$

v and m trade off negatively with each other, and different combinations of values will fit a given river profile. In Angola, this relationship has been calibrated for westward draining rivers since the Bié dome has a minimum post-Pliocene uplift rate of 0.3 mm yr^{-1} at the coast [*Guiraud et al.*, 2010]. If $n = 1$ and $m = 0.35$, we obtain $v = 3.62$ and can constrain $\partial z/\partial t$, the local incision rate. If different values of m are chosen, $v \approx 1.46 \times 10^4 (4.96 \times 10^{-11})^m$.

All three profiles are adequately fitted using an uplift rate history, which suggests that the Bié dome grew in at least two phases. Uplift commenced around 30–40 Ma at a rate of 0.05–0.1 mm yr^{-1}. A second phase of uplift starts at ~10 Ma, reaching a peak of 0.3 mm yr^{-1} at 5 Ma (Figure 8). Both phases are consistent with a history of uplift determined from onshore and offshore geologic observations [*Jackson et al.*, 2005; *Guiraud et al.*, 2010].

In Figures 9–11, the way in which residual misfit varies as a function of each erosional parameter is systematically investigated for river profiles with different lengths (Barroso, Ngunza, and Limpopo). *Pritchard et al.* [2009] argued that n is probably ~1 since there is little evidence that shock wave behavior occurs along trunk rivers and their tributaries. If shock waves do occur, knickzone retreat could erase parts of uplift rate histories, and reconstructed records would contain gaps [*Pritchard et al.*, 2009; *Royden and Perron*, 2013]. We carried out a series of inversions for each river with n permitted to vary between 0 and 2. When inversions are carried out over a 50–100 Myr interval, a global minimum occurs at $n = 1$. Its position does not vary for different degrees of smoothing and/or of discretization.

Figures 9–11 show that river profiles are best fitted if $m = 0.3$–0.5, which fall within the published range [e.g., *Schoenbohn et al.*, 2004]. Increasing v displaces uplift events closer toward the present day since rates of knickzone retreat depend upon vA^m. Finally, residual misfit varies weakly with A because of the fractional exponent. Thus, A can change without seriously affecting our results. This observation suggests that solutions are not unduly sensitive to slow migration of drainage divides or to moderate river capture events. There is limited evidence that A can rapidly change. For example, the upper reaches of the Zambezi River were probably captured in Plio-Pleistocene times, which doubled the catchment area and the sedimentary flux [*Walford et al.*, 2005]. On the other hand, there is also evidence which from southern Africa that drainage configurations of the Orange and Vaal Rivers were established in Late Cretaceous times and have remained largely unchanged [*Partridge and Maud*, 1987; *Dollar*, 1998; *De Wit*, 1999].

2.4. Uplift as Function of Time and Space

In general, the assumption of spatially uniform uplift cannot be valid, and U varies as a function of both time and space. In principle, knickzones can form at any location along a river profile. For single profiles, spatial and temporal patterns of uplift rate are indistinguishable. However, we can apply the method described by *Roberts et al.* [2012a] which simultaneously inverts multiple river profiles. Critically, this approach enables spatial and temporal signals to be distinguished.

First, we define the loci of vertices within an $X \times Y \times T$ grid, where X, Y, and T are the number of spatial and temporal nodes, respectively. Secondly, a starting uplift rate history is chosen. For simplicity, we use a flat plane, upon which a grid of uplift rate values are set to zero. At any given time, the spatial variation of uplift rate along a given river profile is bilinearly interpolated from this grid. During the inversion procedure, an uplift rate history is sought that smoothly varies through time and space.

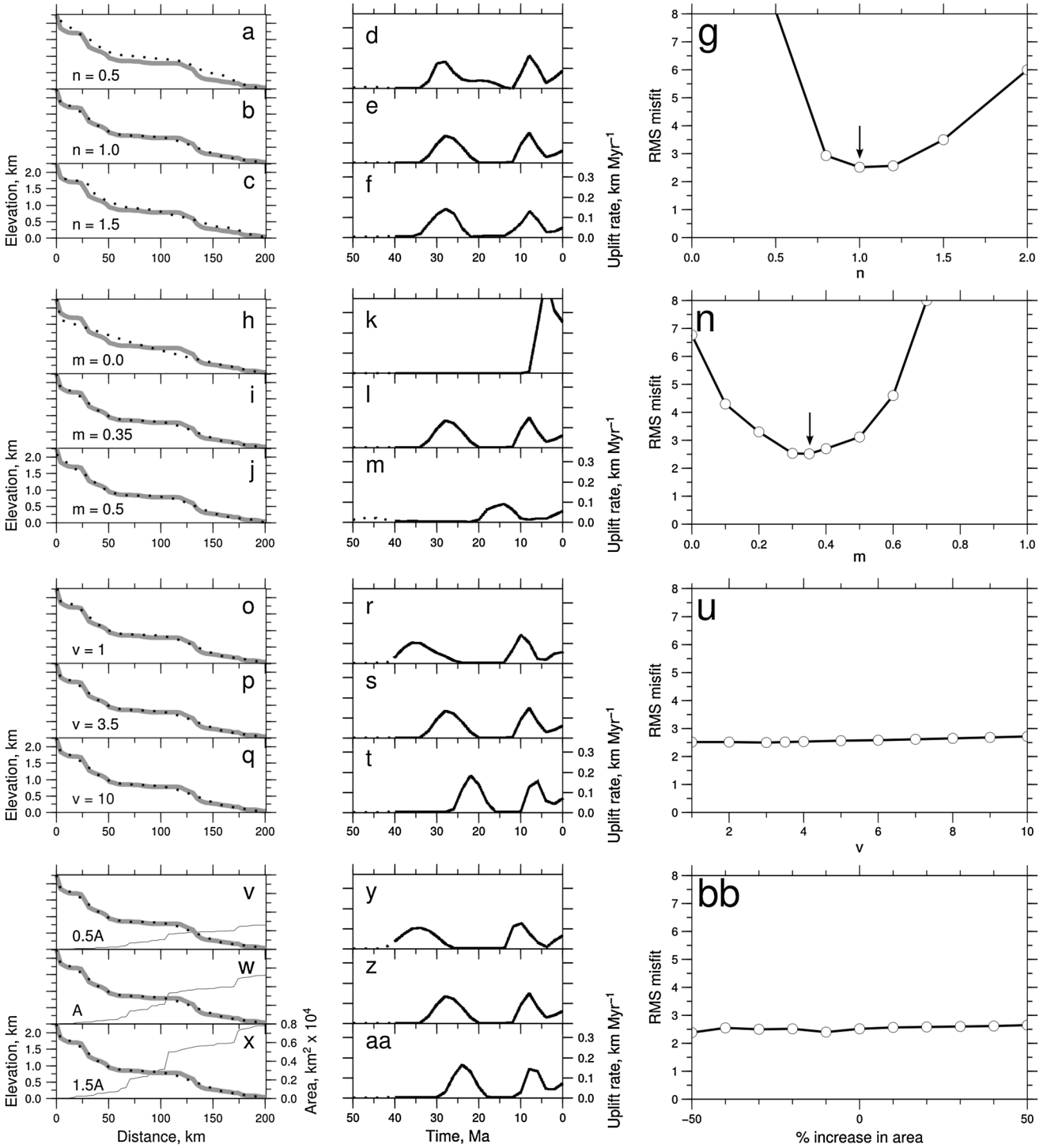

Figure 9. Erosional parameter testing for Barroso River. (a–g) *n* was varied systematically to determine value that yields smallest residual misfit between observed and predicted river profile. In Figures 9a–9c, different values of *n* change predicted river profile. Gray line = profile of Barroso River; dotted line = predicted river profile. Value of *n* in each case is shown at bottom left. In Figures 9d–9f, calculated uplift rate histories for best fitting theoretical river profiles shown in adjacent panels (dotted lines = unreliable uplift rate histories due to breakdown of assumption of spatially invariant uplift). In Figure 9g, misfit between theoretical and observed river profiles as function of *n*. Note position of global minimum at $n = 1$ marked by vertical arrow. (h–n) Analogous tests for varying *m*. Note global minimum at $0.2 \leq m \leq 0.4$. (o–u) Tests for varying *v* between 1 and 10 that fit observations equally well. Note systematic younging of predicted uplift events as *v* increases. (v–bb) Tests for varying *A* by 0.5*A*–1.5*A*. Note trade-off between *A* and *v*.

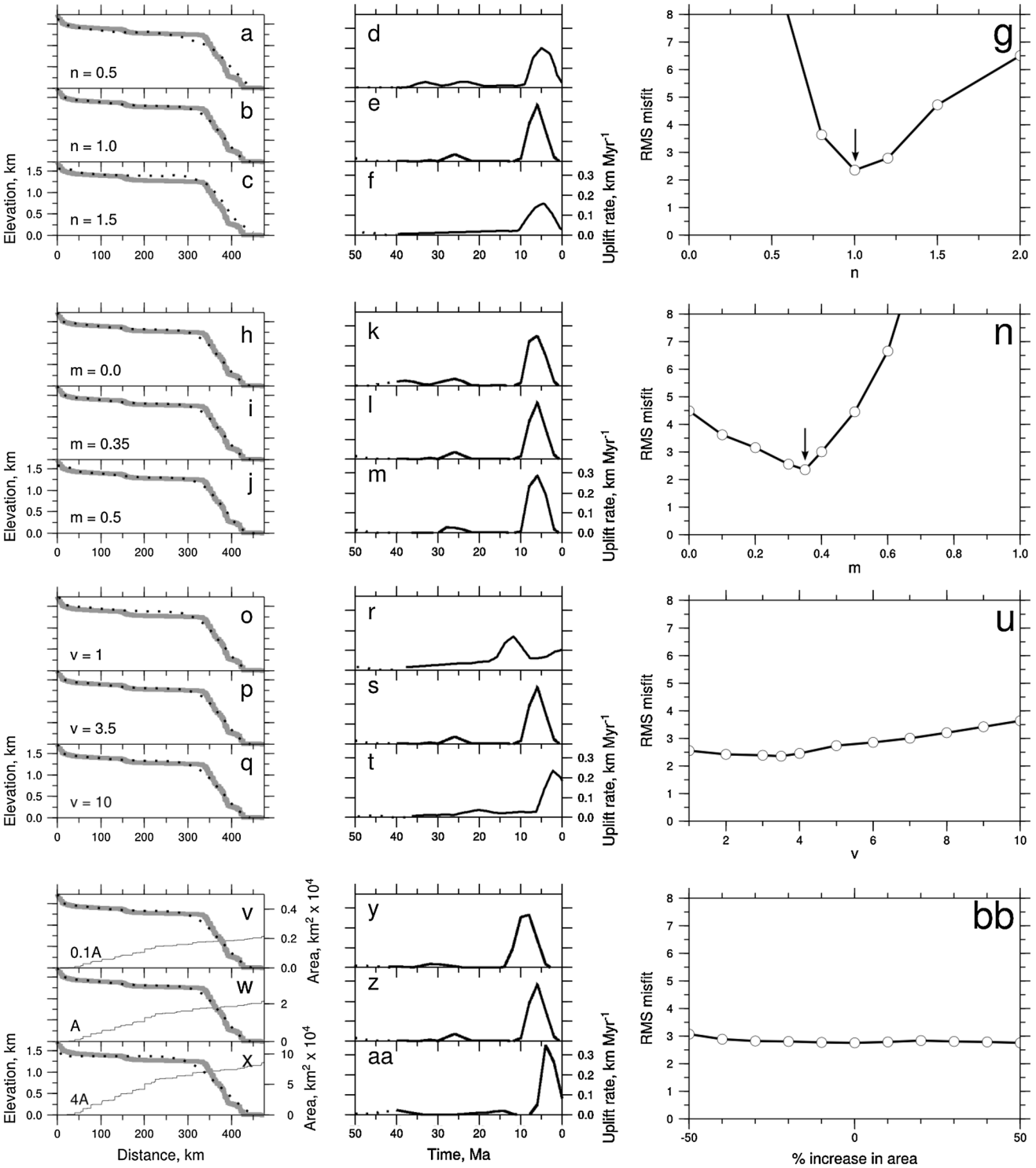

Figure 10. Erosional parameter testing for Ngunza River. (a–g) *n* was varied systematically to determine value that yields smallest residual misfit between observed and predicted river profile. In Figures 10a–10c, different values of *n* change predicted river profile. Gray line = profile of Ngunza River; dotted line = predicted river profile. Value of *n* in each case is shown at bottom left. In Figures 10d–10f, calculated uplift rate histories for best fitting theoretical river profiles shown in adjacent panels (dotted lines = unreliable uplift rate histories due to breakdown of assumption of spatially invariant uplift). In Figure 10g, misfit between theoretical and observed river profiles as function of *n*. Note position of global minimum at $n = 1$ marked by vertical arrow. (h–n) Analogous tests for varying *m*. Note global minimum at $0.2 \leq m \leq 0.4$. (o–y) Tests for varying *v* between 1 and 10 that fit observations equally well. Note systematic younging of predicted uplift events as *v* increases. (v–bb) Tests for varying *A* by 0.1*A*–4*A*. Note trade-off between *A* and *v*.

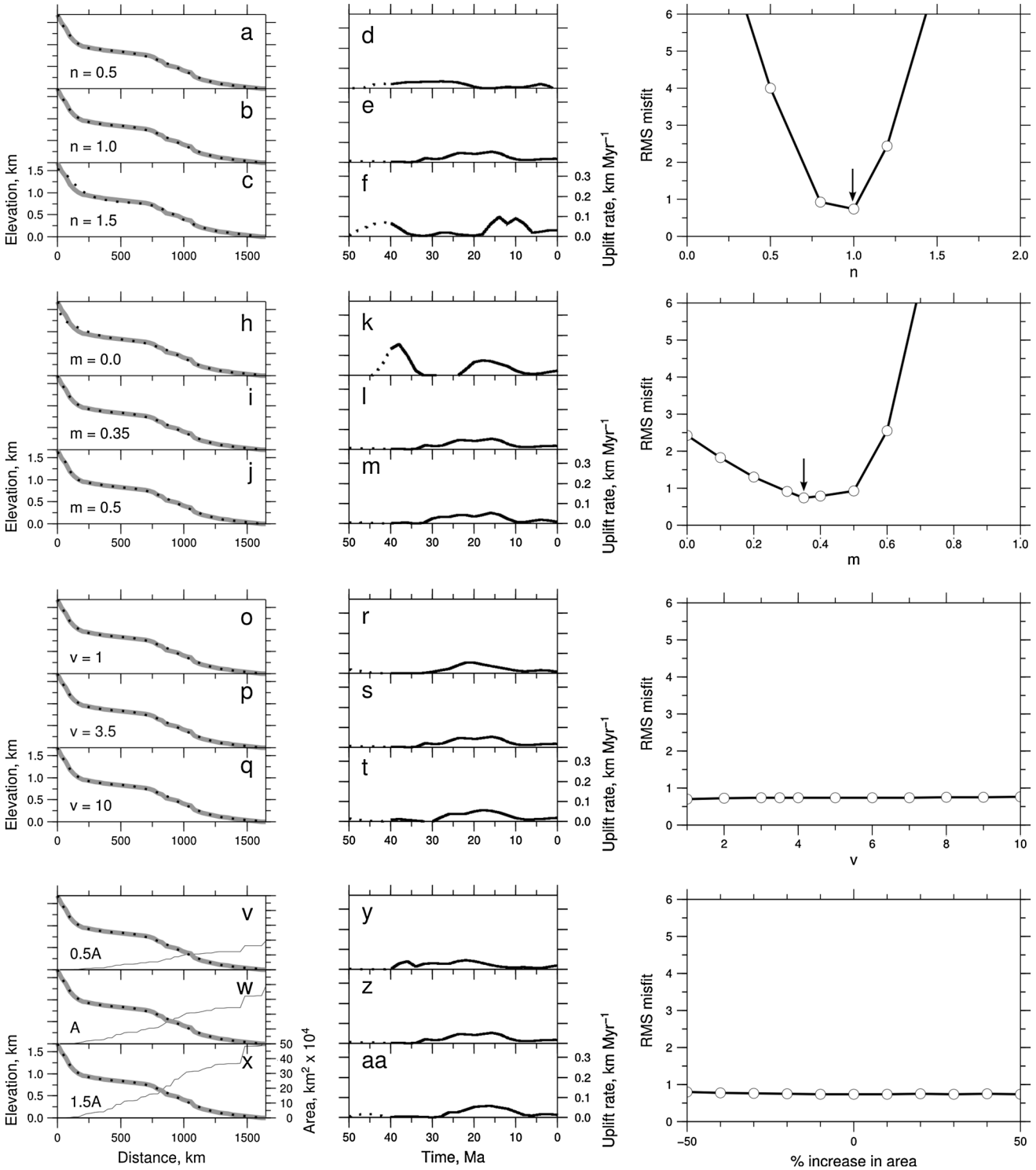

Figure 11. Erosional parameter testing for Limpopo River. (a–g) *n* was varied systematically to determine value that yields smallest residual misfit between observed and predicted river profile. In Figures 11a–11c, different values of *n* change predicted river profile. Gray line = profile of Limpopo river; dotted line = predicted river profile. Value of *n* in each case is shown at bottom left. In Figures 11d–11f, calculated uplift rate histories for best fitting theoretical river profiles shown in adjacent panels (dotted lines = unreliable uplift rate histories due to breakdown of assumption of spatially invariant uplift). In Figure 11g, misfit between theoretical and observed river profiles as function of *n*. Note position of global minimum at $n = 1$ marked by vertical arrow. (h–n) Analogous tests for varying *m*. Note global minimum at $0.2 \leq m \leq 0.4$. (o–u) Tests for varying *v* between 1 and 10 that fit observations equally well. Note systematic younging age of predicted uplift events as *v* increases. (v–bb) Tests for varying *A* by 0.5*A*–1.5*A*. Note trade-off between *A* and *v*.

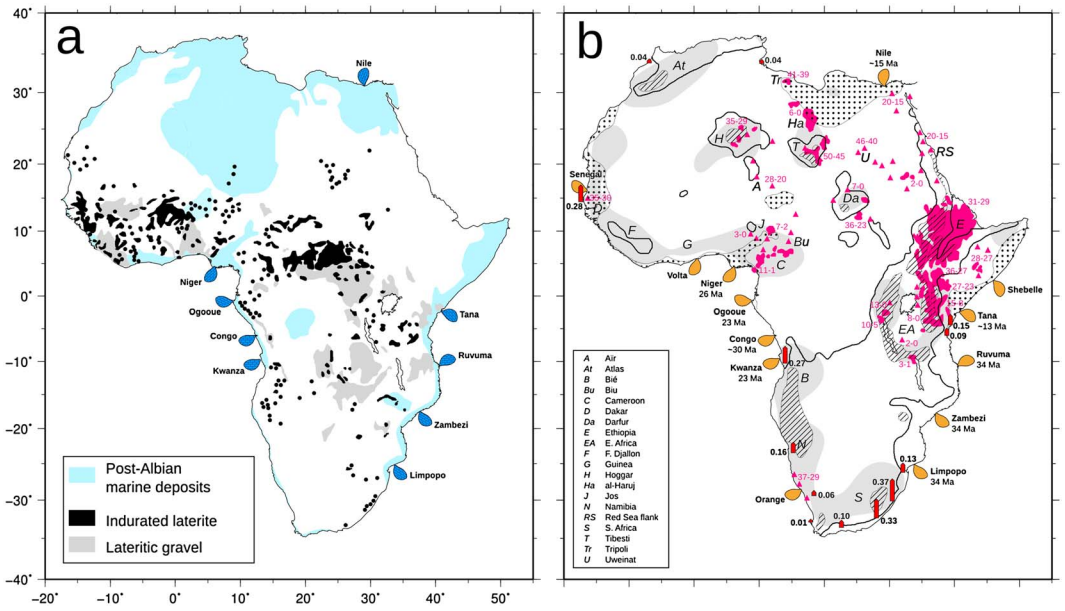

Figure 12. (a) Pre-Oligocene paleogeography of Africa. Blue shading = minimum extent of Cenomanian marine deposition [*Sahagian*, 1988]; black shading = distribution of indurated laterite during Paleogene times [*Burke and Gunnell*, 2008]; gray shading = distribution of lateritic gravels; blue lobes at coastline = major deltas with Paleogene carbonate reef deposits [*Nyagah*, 1995; *Salman and Abdula*, 1995; *Séranne and Nzé Abeigne*, 1999; *Ismail et al.*, 2010]. (b) Early Neogene paleogeography of Africa. Red triangles/shading = dated volcanic craters/flows [*Thorpe and Smith*, 1974; *Ebinger et al.*, 1989; *Reid et al.*, 1990; *Woolley*, 2001; *Liégeois et al.*, 2005; *Permenter and Oppenheimer*, 2007; *McDougall and Brown*, 2009]; warping of Cenomanian surface represented by stippled pattern < 0 km, black line = 1 km, and hatching >2 km [*Sahagian*, 1988]; gray shading = $>$ 10 mGal long-wavelength free-air gravity anomaly; brown lobes at coastline = major deltas showing age of onset of clastic deposition [*Sestini*, 1989; *Nyagah*, 1995; *Salman and Abdula*, 1995; *Séranne and Nzé Abeigne*, 1999; *Anka and Séranne*, 2004; *Reijers*, 2011]; numbered red arrows = radiometrically dated marine deposits with average uplift rate given in mm yr^{-1} [*Partridge and Maud*, 1987; *Odada*, 1996; *Partridge*, 1998; *Van der Wateren and Dunai*, 2001; *Roberts and Brink*, 2002; *Elmejdoub and Jedoui*, 2009; *Guiraud et al.*, 2010].

We have chosen to minimize a trial function, H, where

$$H = \chi^2 + \mu\|m\| + w_1 \iiint f\,dx\,dy\,dt \tag{5}$$

and

$$\chi^2 = \left[\frac{1}{NM}\sum_{n,m=1}^{N,M}\left(\frac{z_{nm}^o - z_{nm}^c}{\sigma_n}\right)^2\right]^{1/2}. \tag{6}$$

The observed and calculated river profiles are z_i^o and z_i^c, N is the number of data points along each river, M is the number of rivers, and σ_n is the uncertainty in river profile elevation. The Lagrangian multiplier is μ (i.e., regularization parameter), $\|m\|$ is the model norm, f is the positivity constraint (e.g., $f = \cosh U - 1$ for $U < 0, f = 0$ for $U \geq 0$), and w_1 is its weighting coefficient. Our aim is to find a smooth distribution of U that minimizes χ^2 for a collection of river profiles. An optimal model (i.e., the "smallest model") is defined by $\|m\|$, which ensures that all spatial and temporal gradients and curvatures are smooth.

There is a well-known negative trade-off between model smoothness and model fit [*Parker*, 1994]. Improved resolution can only be obtained by degrading statistical reliability. There is no single optimal solution, but it is important to seek the smoothest model that yields the smallest misfit. μ acts to smooth first and second derivatives of $U(x, y, t)$ through space and time. When μ is increased, the model norm, $\|m\|$, decreases, and the data misfit, χ^2, increases. An optimal degree of smoothing is determined by systematically varying μ.

Our starting assumption of a flat plane implies that the African landscape was low lying during Paleogene times (Figure 12a) [*Burke and Gunnell*, 2008; *Partridge*, 1998]. There are four important lines of evidence to support this inference. The distribution of post-Albian marine deposits shows that large portions of

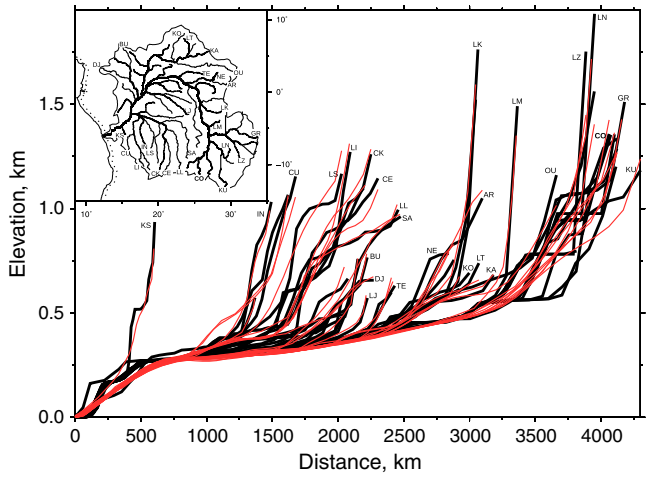

Figure 13. Inverse modeling of 53 river profiles from Congo catchment (see inset). Labeled black lines = observed river profiles; red lines = calculated river profiles (Table AI). Cumulative residual misfit, $\chi^2 = 2.66$.

North and East Africa were below sea level [*Sahagian*, 1988]. During Eocene times, widespread laterites and lateritic gravels covered the continent, notably between 20°N and 30°S. The existence of thick laterites suggests that topographic gradients were modest [*Burke and Gunnell*, 2008]. Carbonate reef deposits fringed several African deltas during Paleogene times, which is consistent with negligible clastic deposition

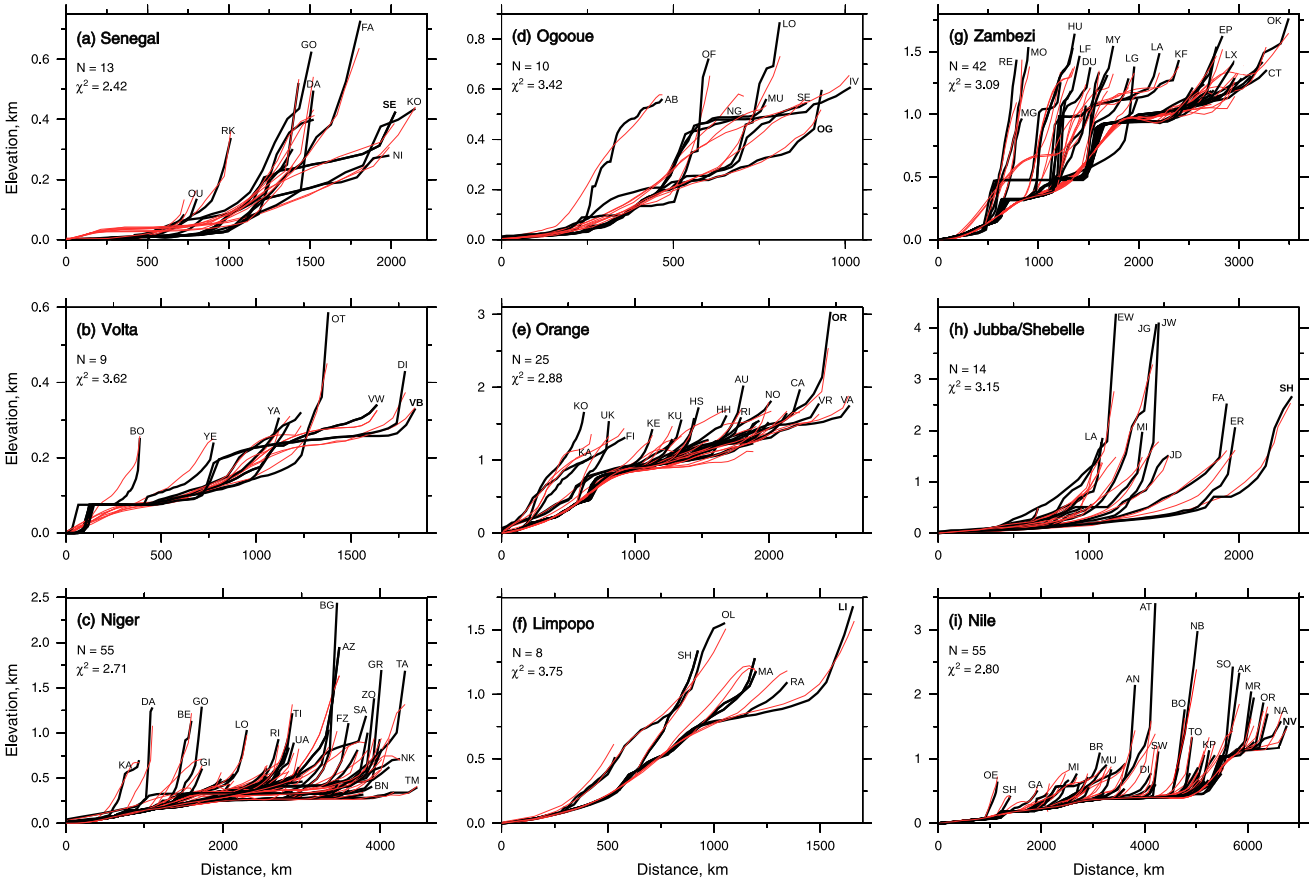

Figure 14. Inverse modeling of river profiles from nine major African catchments (Figure 2a). In each case, labeled black lines = observed river profiles; red lines = calculated river profiles; χ^2 = cumulative residual misfit; N = number of river profiles (Table AI).

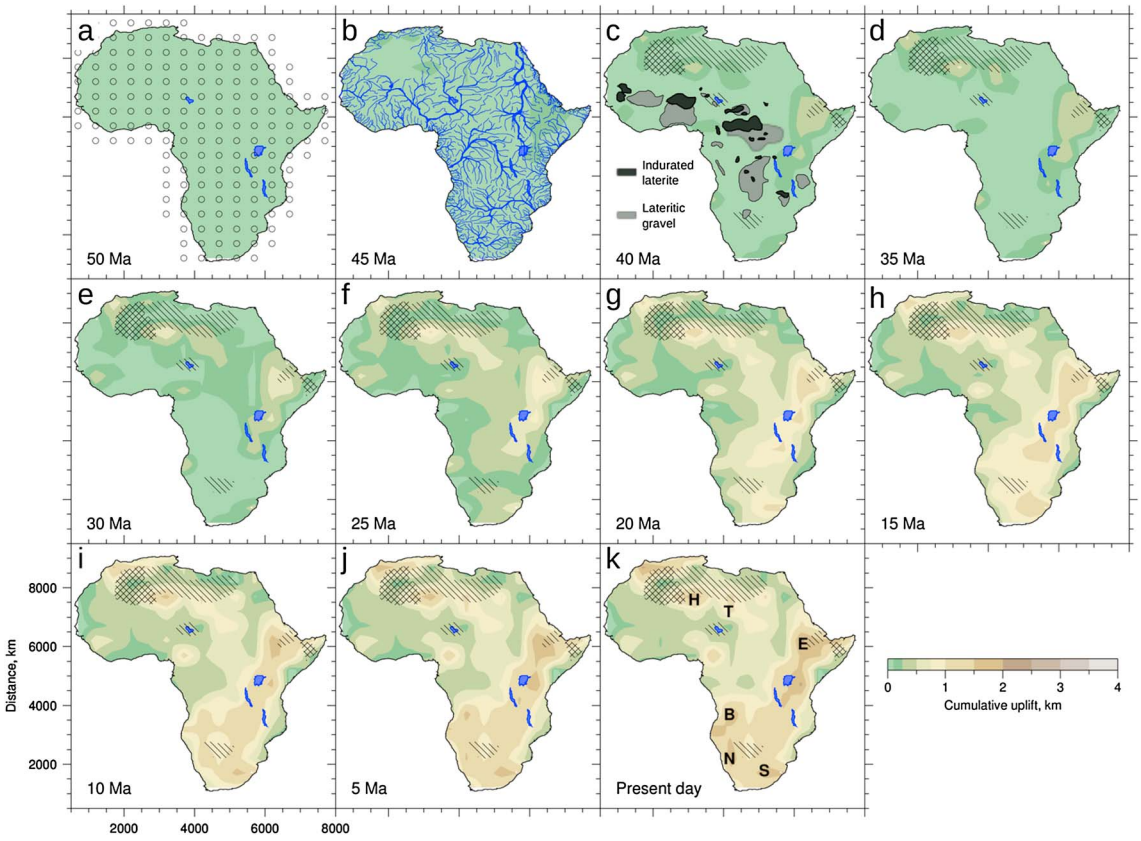

Figure 15. Cumulative uplift history of Africa (i.e., $\int_o^t U(x, y, t)\,dt$). (a) Initial topography at 50 Ma. Circles = vertices at which uplift rate can vary during inversion. (b) Spatial pattern of uplift at 45 Ma. Blue lines and patches = rivers of Strahler order ≥ 5 and lakes, respectively. (c) Spatial pattern of uplift at 40 Ma and distribution of indurated laterite and lateritic gravel. Cross-hatching = regions where drainage networks cannot be reliably recovered; hatching = regions where recovered uplift rate history is unreliable due to effects of internal drainage and/or poor drainage recovery. (d–k) Snapshots of spatial pattern of uplift from 35 Ma to present day. H = Hoggar; T = Tibesti; E = Ethiopian Highlands; B = Bié Dome; N = Namibian Dome; S = South African Plateau.

(Figure 12a). This prolonged period of tectonic quiescence was terminated by a burst of widespread magmatism, which started at ~40 Ma and has continued to the present day. Cenomanian surfaces and lateritized peneplains were warped during Neogene times [*Sahagian*, 1988]. This abrupt change was accompanied by rapid increases in clastic efflux at various deltas (Figure 12b).

We have simultaneously inverted 710 river profiles as a function of uplift rate history over the last 50 Myr (Table AI; Figures 13–15). In order to make this problem computationally tractable, digitized river profiles were decimated. Profiles longer or shorter than 1000 km were sampled every 200 km or 20 km, respectively. and we set up a coarse grid of uplift rate values through space and time (500 km × 500 km × 2.5 Myr). This grid structure has 174 spatial and 21 temporal nodes.

Our goal is to minimize the misfit between observed and calculated river profiles selected from 10 major catchments and from >400 smaller rivers. River profiles from the Congo catchment are shown in Figure 13. These 53 tributary profiles have been simultaneously fitted as part of an Africa-wide inversion (Table AI). Observed and calculated profiles for rivers and tributaries from the other nine major catchments are shown in Figure 14. Given the degree of decimation and the coarseness of our spatial and temporal gridding, cumulative residual misfits between observed and calculated profiles are small ($\chi^2 \sim 2.7$).

A cumulative uplift history of Africa (i.e., the integrated uplift rate through time, $\int_o^t U(x, y, t)\,dt$) obtained by inverse modeling is shown in Figure 15. This history suggests that modern African topography grew during the last 30–40 Myr, in accordance with a suite of geologic observations. There are two distinct phases of growth. During the first phase, the Hoggar, Tibesti, and Afar swells began to develop at 35–40 Ma, which is consistent with their magmatic histories [e.g., *Woolley*, 2001; *Liégeois et al.*, 2005]. Growth of the Afar swell quickly outstripped the rest, spreading south along the nascent East African Rift with a peak uplift rate

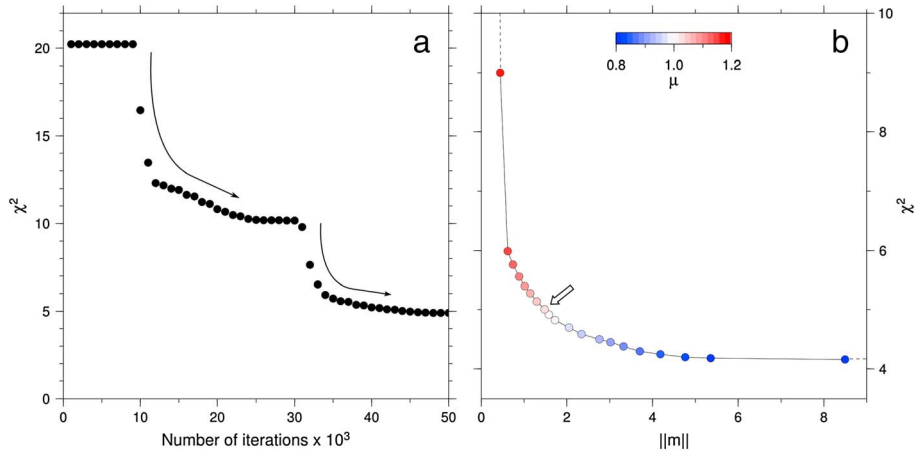

Figure 16. (a) Root-mean-square misfit, χ^2, as a function of 50,000 iterations. Starting and final values of χ^2 are 20.1 and 4.6, respectively. Optimization carried out using conjugate gradient method from *Press et al.* [1992], which produces rapid decreases in χ^2 indicated by arrows. (b) Data misfit, χ^2, as function of model misfit, $||m||$. Colored circles = different inversions where color gives values of damping factor, μ, applied through space and time; arrow at $\mu = 1.04$ indicates smoothest model that yields best fit.

of ~0.15 mm yr^{-1}. A second phase migrated into subequatorial Africa and occurred on two wavelengths. Long-wavelength uplift of the plateau started at 20 Ma at rates of 0.01–0.10 mm yr^{-1}. The Bié, Namibian, and South African swells grew rapidly over the last 10 Ma at rates of up to 0.15 mm yr^{-1}.

An important question concerns resolution of the cumulative rate history shown in Figure 15. We have tried to ensure that the distribution of uplift through space and time does not overfit the drainage inventory by seeking the smoothest distribution that yields the smallest misfit (Figure 16). We tested a suite of models in which μ has been systematically varied (Figure 16b). An appropriate balance between smoothness and misfit is achieved for $\mu \sim 1.04$. During a typical optimization, χ^2 decreases from 20.1 to 4.6.

Figures 17a and 17b summarize the quality of fit between calculated and observed river profiles. In general, the degree of misfit is small, especially for the longest river profiles (e.g., Nile, Congo, Niger, and Zambezi). Shorter river profiles are sometimes fitted less well, especially if they have sharp knickzones. In some instances, large misfits could indicate that important assumptions (e.g., invariant upstream drainage area) are violated. For example, river capture events triggered by initiation of rift flank uplift along the Red Sea margin could be responsible for poor fits to Nile tributaries that drain the Ethiopian Highlands [*Macgregor*, 2012]. The calculated present-day topography represents an upper bound estimate on African topography (i.e., it is a snapshot of the landscape prior to dissection by erosive processes). Therefore, it is appropriate to compare this surface with a summit envelope surface constructed by fitting loci of present-day drainage divides. Figures 17c and 17e show that these two surfaces are in good agreement. We find that 60% is accurate to within ±0.1 km of the summit envelope, and 90% of the calculated topography agrees to within ±0.25 km (Figure 17f).

2.5. Shock Waves

There is much discussion in the geomorphologic literature concerning the value of *n*. *Whipple and Tucker* [1999] demonstrated that different values of *n* modify the calculated shape of a river profile for a given uplift history. Slope-area analyses of river profiles, which estimate m/n, have been used to argue that $n > 1$, although this argument depends on the chosen value of *m*. *Roberts et al.* [2012b] showed that slope-area analysis is highly susceptible to random noise and that m/n cannot be reliably retrieved in this way. *Pritchard et al.* [2009] argued that a shock occurs if the steeper reach of the river overtakes a less steep reach, which is propagating upstream at a lower speed. If vA^m is approximated by $v_\circ x^m$ and if *L* is the length of the river, they showed that a shock forms within the domain $0 \le x \le L$ if, and only if,

$$\left(\frac{n-1}{n}\right)\frac{dU}{dt} > (n-m)v_\circ^{1/n}L^{m/n-1}\,[U(t)]^{2-1/n} \tag{7}$$

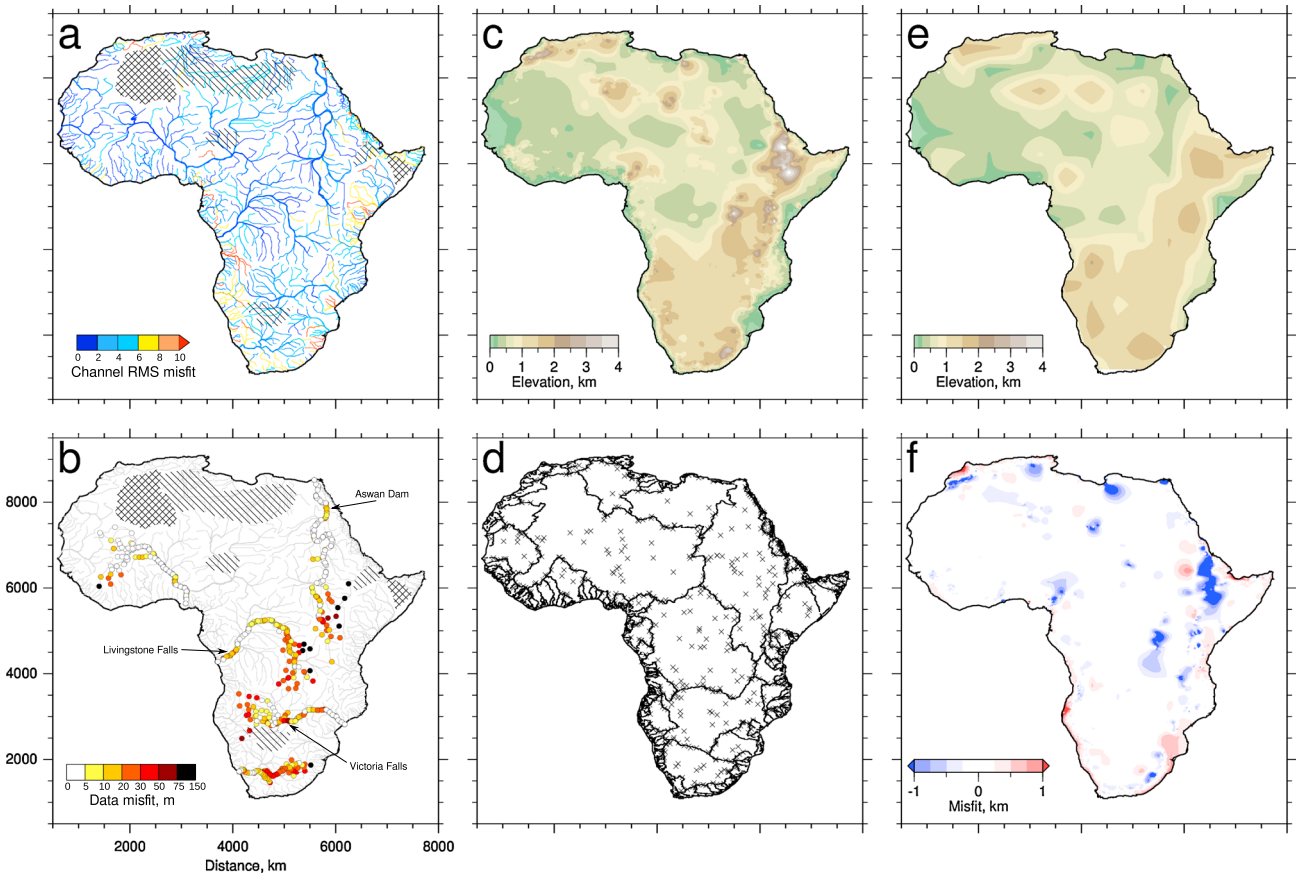

Figure 17. (a) Residual misfit between predicted and observed river profiles. (b) Spot values of residual misfit along principal river profiles. (c) Calculated summit envelope (i.e., surface fit through loci of present-day drainage divides). (d) Network of present-day drainage divides used to calculate summit envelope. Crosses = loci of 710 river heads. (e) Calculated present-day surface (Figure 15). (f) Difference between predicted and observed summit envelopes.

at some time during uplift. If a shock forms, the river erases part of its uplift rate history, and the reconstructed record contains a gap. *Royden and Perron* [2013] used a different argument to reach the same conclusion.

In one-dimensional inversions, where we seek smooth distributions of $U(t)$, it is straightforward to test how varying n affects the residual misfit (Figures 9–11). A similar approach can be used in three dimensions where we seek $U(x, y, t)$. Figure 18 presents four inverse models that have been run with different values of n. The lowest residual misfit, $\chi^2 = 5.0$, is obtained for $n = 1$. When $n = 0$, $\chi^2 = 9.2$ and the qualitative match between calculated and observed river profiles throughout Africa is surprisingly good. This result suggests that the upstream drainage area, A, is the dominant control on incision rate. When $n > 1$, residual misfits are significantly larger, matches between calculated and observed river profiles are poor, and the calculated present-day cumulative uplift departs from the summit envelope.

2.6. Precipitation

Equation (2) implicitly assumes that average discharge along a river channel is a function of drainage area. Discharge must also vary as a function of precipitation. Since Late Cretaceous times, atmospheric circulation above Africa has probably been largely static with large areas of high pressure covering northern and southern regions [*Parrish and Curtis*, 1982]. During the Cenozoic Era, the ~10° northward drift of Africa fell within the width of a single Hadley cell (i.e., 20–30°), which controls the distribution of major latitudinal climate zones [*Frierson et al.*, 2007]. Nonetheless, there is some evidence that continent-scale changes in precipitation have occurred during Cenozoic times [e.g., *Partridge and Maud*, 1987; *Feakins and Demenocal*, 2008; *Wichura et al.*, 2010]. For example, regional Oligocene cooling of South Africa, possibly triggered by long-wavelength uplift, might have caused increases in erosion and deposition [*Anka and Séranne*, 2004]. Growth of the East African Rift may have induced orographic precipitation during Miocene times, whereas

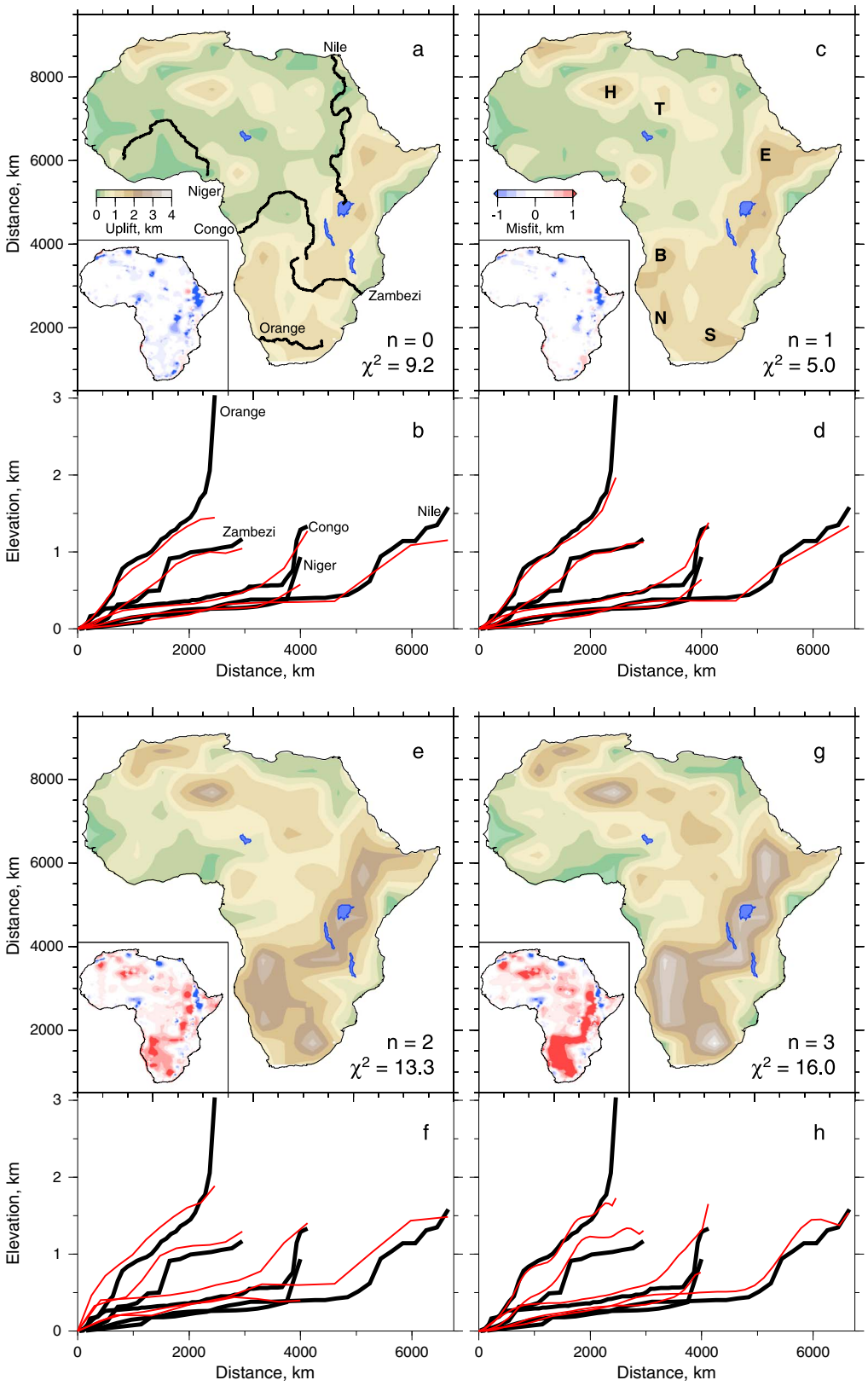

Figure 18. Tests of *n*. (a) Map of present-day cumulative uplift calculated by inversion with $n = 0$. Inset = misfit between observed and calculated topography; χ^2 = cumulative misfit between 710 observed and calculated river profiles. (b) Five observed (black) and calculated (red) river profiles; (c and d) same as Figures 18a and 18b but for $n = 1$; (e and f) same as Figures 18a and 18b but for $n = 2$; (g and h) same as Figures 18a and 18b but for $n = 3$.

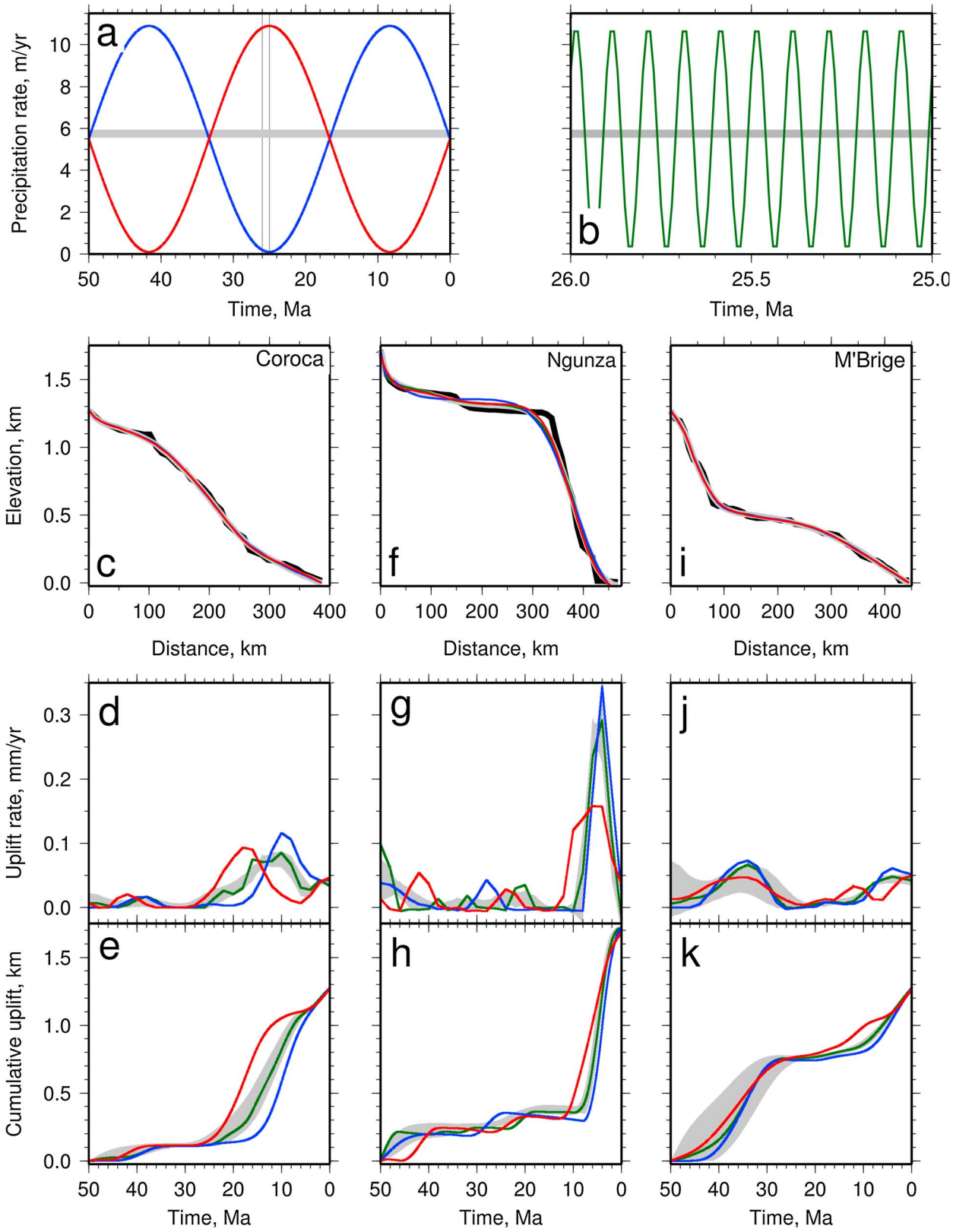

Figure 19. One-dimensional precipitation tests for river profiles from Bié dome. (a, b) Precipitation rate variations (blue/red = 0.03 Myr^{-1}; green = 10 Myr^{-1}). Gray bar = average precipitation rate; vertical lines in Figure 19a = range of Figure 19b. (c) Black line = Coroca River; colored lines = calculated river profiles for different precipitation rate variations. (d, e) Corresponding uplift histories. Gray band = uplift history from *Monte Carlo* inversions (see Figure 8). (f–h) Ngunza River analyses. (i–k) M'Brige River analyses.

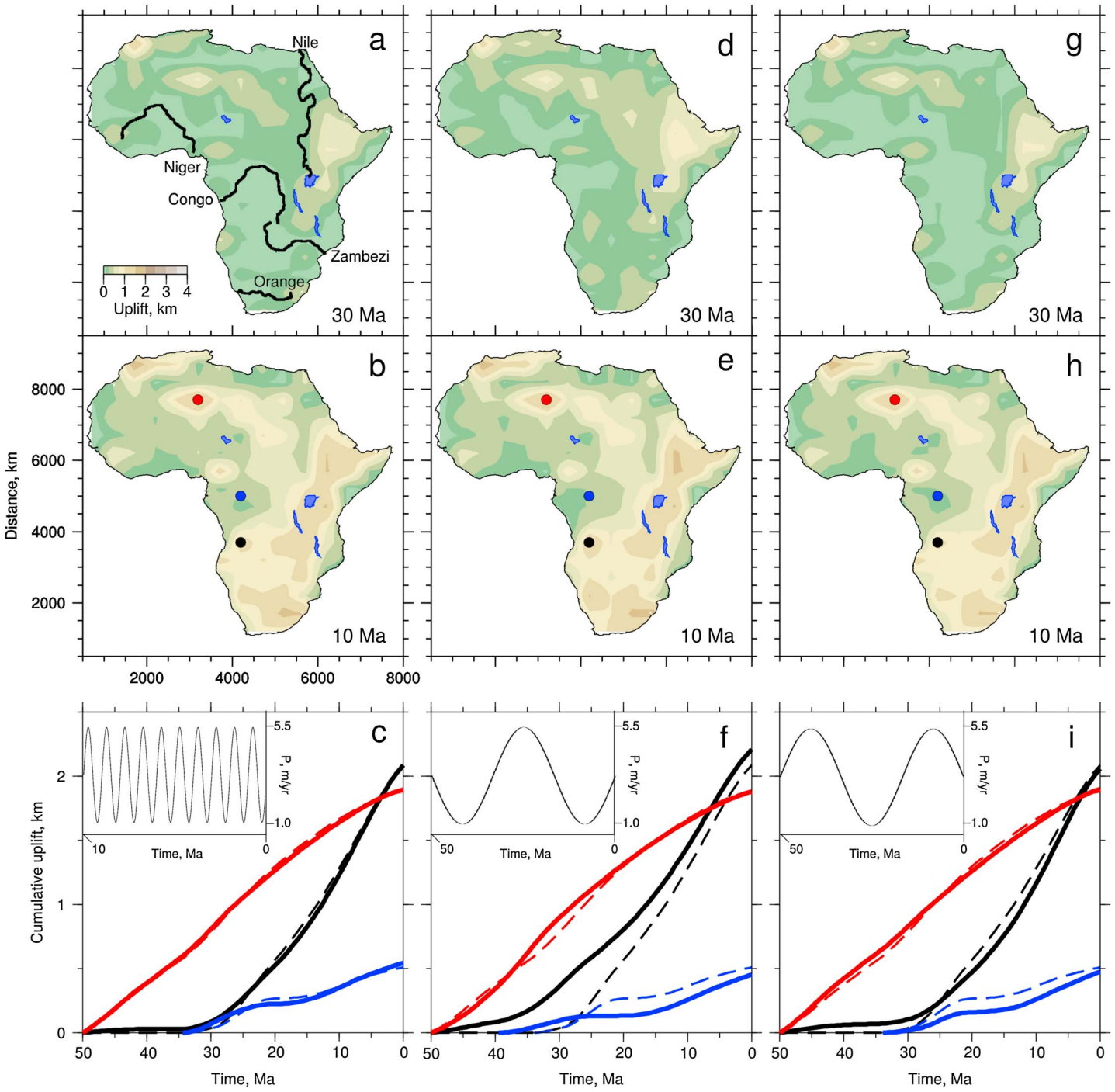

Figure 20. Two-dimensional precipitation tests for all 710 river profiles. (a, b) Cumulative uplift maps calculated at 30 and 10 Ma for precipitation rate which varies with frequency of 1 Myr^{-1}. (c) Cumulative uplift as function of time at three colored nodes. Solid lines = varying precipitation; dashed lines = constant precipitation. Inset = precipitation variation. (d, e) Cumulative uplift maps for dry-wet-dry cycle (frequency of 0.03 Myr^{-1}). (f) Cumulative uplift as function of time as before. Inset = precipitation variation. (g, h) Cumulative uplift maps for wet-dry-wet cycle (frequency of 0.03 Myr^{-1}). (i) Cumulative uplift as function of time as before. Inset = precipitation variation.

intensification of the Asian Monsoon (9–6 Ma) may have caused a reduction in East African precipitation rates [*Feakins and Demenocal*, 2008; *Wichura et al.*, 2010].

Mean annual rainfall varies from <0.001 m yr^{-1} in parts of the Sahara Desert to >5 m yr^{-1} in tropical rain forests [*Nicholson*, 2001]. Present-day aridity of the Sahara contrasts with higher Holocene precipitation rates recorded by freshwater algae, by paleosols, and by fluvial and lacustrine sedimentary rocks

(e.g., 150–400 mm greater than today) [*Kröpelin and Soulié-Märsche*, 1991]. Sparse records, such as distribution of organic-rich sapropel deposits and terrigenous dust in marine sediments, have been used to reconstruct Cenozoic precipitation [e.g., *Feakins and Demenocal*, 2008]. These reconstructions suggest that precessionally driven changes of insolation provided the fundamental pacing of humid-arid cycles during Miocene and Pliocene times [*Feakins and Demenocal*, 2008]. On longer timescales, leaf morphology has been used to suggest that arid regions of Africa have been wetter (e.g., ~0.5–1 m yr^{-1} during Eocene times) [*Jacobs and Herendeen*, 2004].

Even in the absence of a comprehensive history of precipitation rate, we can usefully explore how different periodicities and amplitudes of precipitation rate affect calculated uplift rate histories. Following *Roe et al.* [2002] and *Wu et al.* [2006], equation (2) is recast as

$$E(x,t) = -v_{\circ} Q^m \frac{\partial z}{\partial x}, \tag{8}$$

where $Q(x,t) = p(t) \times A(x)$ is discharge as a function of time and distance along a river and $p(t)$ is the rate of precipitation. Here we assume that

$$p(t) = p_{\circ} + S\sin(2\pi\omega t), \tag{9}$$

where ω is frequency. Constants are $p_{\circ}$ and S, which ensure that $p(t) \geq 0$ (i.e., $p_{\circ} \geq S$).

In Figure 19, we have inverted three river profiles to determine how uplift rate varies as a function of time for different histories of precipitation rate. In each case, $v_{\circ}$ was chosen to ensure that $vA^m \approx v_{\circ}Q^m$ when $p(t) = p_{\circ}$. Uplift rate histories were calculated for different precipitation rates, which varied from 0 to 12 m yr^{-1} with periods of 0.1 Myr to 30 Myr. These values were chosen to reflect the likely range of Eocene to Recent precipitation rates, including modern-day extrema [*Nicholson*, 2001; *Feakins and Demenocal*, 2008; *Milliman and Farnsworth*, 2011]. Recovered uplift rate histories are indistinguishable when precipitation rate varies with periods as long as 1 Myr. We conclude that orbital forcing of humid-arid cycles does not significantly affect our results. Longer-period variations in precipitation rate (e.g., 30 Myr) are more important because knickzone retreat velocities speed up and slow down as a function of time and distance upstream. In a wet-dry-wet precipitation cycle that lasts for 50 Ma, all three river profiles are matched, but peak uplift rates are shifted toward the present day, compared with a constant precipitation model. In a dry-wet-dry cycle, peak uplift rates are shifted backward in time. These time shifts are small, given the amplitude and frequency of precipitation changes. Similar results were obtained for Africa-wide inverse models (Figure 15). Thus, short period (i.e., orbitally modulated) changes in precipitation rate have little effect on cumulative uplift histories. Long-period (e.g., wet-dry-wet and dry-wet-dry) cycles are more important, but even they do not dramatically alter our results (compare, for example, Figures 15e and 15i, Figures 20d and 20e, and Figures 20g and 20h).

3. Geologic Calibration

Three categories of geologic and geophysical observations were used to check the results of inverse modeling. First, it is generally accepted that African topography was subdued during Paleogene times when thick lateritic deposits draped large swathes of the continent (Figure 12a). This observation implies that the bulk of modern African topography developed during the last 30 Myr. The present-day position of pre-Cenozoic marine strata provides a useful indication of areas that have experienced later uplift [*Sahagian*, 1988] (Figure 12b). Secondly, widespread magmatism began at 30–40 Ma. This magmatism was generated by subplate convective circulation, which probably played a central role in generating Africa's basin-and-swell physiography during the Neogene Period. Thirdly, certain convective swells, especially in subequatorial Africa, intersect coastlines where uplifted marine deposits provide independent estimates of regional uplift.

Intraplate Cenozoic volcanism in Africa is largely restricted to intercratonic areas [*Thorpe and Smith*, 1974]. Predicted episodes of uplift correlate reasonably well with periods of more intense magmatic activity in Hoggar, Tibesti, and Afar (Figures 12b, 21a, and 21c) [*Liégeois et al.*, 2005; *Thorpe and Smith*, 1974]. In the Afar region, the most rapid uplift occurred between 40 and 30 Ma when widespread flood basalts spread across the Ethiopian Plateau [*Beccaluva et al.*, 2011]. Between 30 Ma and the present day, both predicted uplift and magmatism young southward along the East African Rift (Figure 12b) [*McDougall and Brown*, 2009]. *Veldkamp et al.* [2007] and *Wichura et al.* [2010] reconstructed Pliocene lava flows from the East African Rift

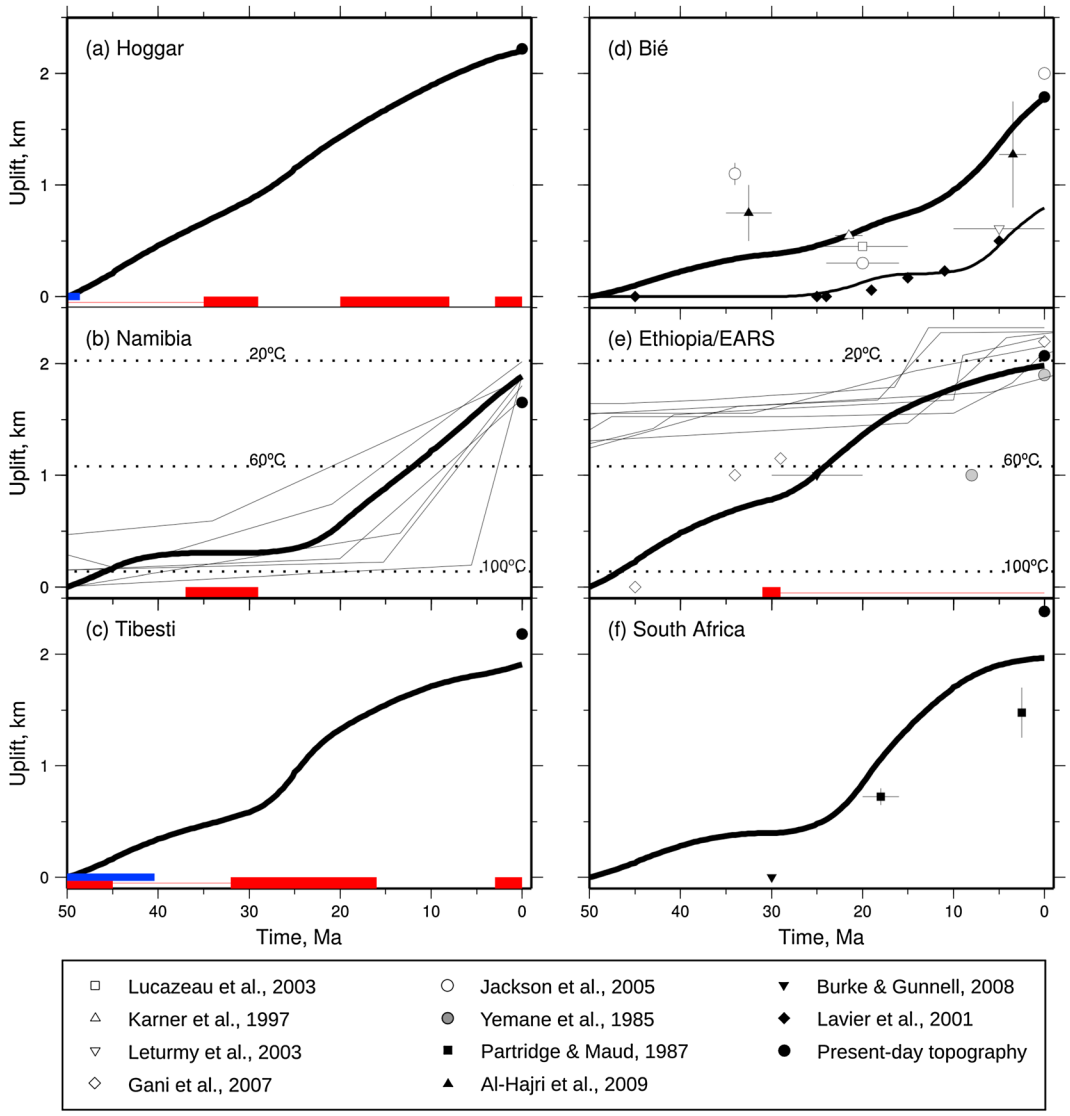

Figure 21. Observed and calculated uplift histories for six topographic swells. Thick black lines = cumulative uplift history at swell center; solid circles = present-day height at swell center; other symbols = independent geologic estimates of uplift/denudation; red bars/lines = magmatic activity [*Reid et al.*, 1990; *Woolley*, 2001; *Liégeois et al.*, 2005; *Permenter and Oppenheimer*, 2007; *McDougall and Brown*, 2009]. (a, c) Blue bars = periods of marine limestone deposition [*Goudarzi*, 1970; *Swezey*, 2009]. (b) Thin black lines = crustal cooling estimates from apatite fission track analyses [*Luft et al.*, 2005]; depth of 60°C partial annealing zone indicated as dotted line [*Raab et al.*, 2005]. (d) Thin black line = cumulative uplift history adjacent to uplift estimate of *Lavier et al.* [2001]. (e) Thin black lines = crustal cooling estimates for Rwenzori Mountains, Uganda [*Bauer et al.*, 2013].

and obtained local uplift rates that also match our regional predictions (0.06–0.08 mm yr^{-1}). Volcanic rocks are also useful benchmarks for incision rates. For example, *Gani et al.* [2007] used K-Ar and $^{40}Ar/^{39}Ar$ dating of Cenozoic volcanic rocks to determine long-term incision rates of the Blue Nile, which drains the Ethiopian Plateau. These rates have increased steadily from 30 Ma to the present day. Estimates of net rock uplift since 30 Ma roughly agree with our cumulative uplift history of Afar region at the headwaters of the Blue Nile.

In subequatorial Africa, the South African, Namibian, and Bié swells intersect the coastline. *Partridge* [1998] and *Partridge and Maud* [1987] used the distribution of emergent, and occasionally marine, terraces and raised beaches to suggest that the South African dome was uplifted in a series of discrete episodes during post-Miocene times (Figures 12b and 17). Their uplift estimates are consistent with our predicted uplift history and corroborate *Burke*'s [1996] suggestion that up to 800 m of uplift has occurred since Oligocene times. Radiometric dating of fauna from perched river terrace gravels has yielded post-Pliocene uplift

rates of ~0.35 mm yr^{-1} along the eastern South African coast [*Partridge and Maud*, 1987, 2000]. Along the Western Cape, however, a series of stepped paleoshorelines suggest lower uplift rates of <0.1 mm yr^{-1} [*Roberts and Brink*, 2002]. Thus, a pronounced east-west gradient of uplift rate exists along the coast of southern Africa (Figure 12b). This gradient is reproduced in our topographic growth predictions of the South African swell (Figure 15). Asymmetric uplift is thought to have been centralized along a series of clearly defined axes, which affected Neogene drainage planforms [*Partridge and Maud*, 1987; *Dollar*, 1998; *Partridge and Maud*, 2000].

Along the Angolan margin adjacent to the Bié swell, Plio-Pleistocene uplift rates have been determined by a combination of dating and calibrating of emergent marine terrace deposits [e.g., *Guiraud et al.*, 2010]. Within the exhumed Kwanza basin, *Jackson et al.* [2005] used the biozonation of planktonic foraminifera to identify major hiatuses in marine sedimentation, which are thought to indicate phases of uplift and exhumation. The most important phases occurred during Oligo-Miocene and Plio-Pleistocene times and vary in amplitude along the shelf. Rivers that drain the Bié dome usually have deeply incised middle and upper reaches (e.g., Figure 7a).

Similar evidence for incision is evident along the edge of the Namibian dome, ~1500 km farther south where deep and narrow canyons exist. The 250 m deep Kuiseb Canyon is thought to have resulted from a pulse of high incision rates and headward erosion which started 2.8 Myr ago [*Van der Wateren and Dunai*, 2001]. Biostratigraphical evidence from perched marine deposits, duricrusts, and gravel terraces in this area suggests that an episode of river incision and landscape rejuvenation affected southwest Namibia during Pliocene times [*Smith et al.*, 1993; *Van der Wateren and Dunai*, 2001]. Incision continues today, sculpting Holocene valley silts of the Kuiseb River into dramatic hanging remnants known locally as "castles" [e.g., *Wienecke and Rust*, 1975; *Smith et al.*, 1993]. These observations are consistent with renewed growth of the Namibian dome at ~10 Ma (Figure 15). Pleistocene incision rates of 0.04–0.16 mm yr^{-1}, estimated from ^{21}Ne analyses on terraces and pediment surfaces cut by the Kuiseb River, compare favorably with our predicted uplift rates of ~0.1 mm yr^{-1} (Figures 12 and 15) [*Van der Wateren and Dunai*, 2001].

Figure 21 summarizes these geomorphologic constraints and compares them with predicted cumulative uplift histories of six major swells. Our results can also be compared with thermochronological studies. Many studies have been carried out, especially in southern Africa [e.g., *Brown et al.*, 2002; *Raab et al.*, 2002; *Luft et al.*, 2005; *Raab et al.*, 2005]. There, three major cooling episodes appear to have taken place since Paleozoic times [*Bauer et al.*, 2013]. However, thermochronologic studies generally yield low, or decelerating, rates of Cenozoic cooling. For example, *Tinker et al.* [2008] infer that significant cooling, and therefore rock exhumation, had occurred by Late Cretaceous times due to the paucity of younger tracks. Thermal modeling of fission track data from the Namibian and South African passive margins indicates that a discrete phase of denudation occurred at 130 Ma, possibly associated with opening of the South Atlantic Ocean [*Brown et al.*, 2002]. Since that time, at least 4.5 km of denudation has taken place along the coastal rim of the Drakensberg Escarpment. Renewed denudation of ~0.2 km Myr^{-1} occurred in Late Cretaceous times (~90–70 Myr). During Cenozoic times, denudation rates are as low as <0.02 km Myr^{-1} [*Brown et al.*, 2002; *Raab et al.*, 2005].

Apatite and titanite (U-Th)/He thermochronometry do not necessarily preclude post-Mesozoic uplift and denudation. *Flowers and Schoene* [2010] give an upper bound estimate of 850 m for Cenozoic unroofing, with exhumation rates decelerating toward the present day. However, late Cenozoic cooling and denudation has not been reported from analyses of subsurface apatite grains collected from boreholes [*Brown et al.*, 2002; *Van der Beek et al.*, 2002]. Uplift and partial erosion of the Namibian swell matches rapid exhumation of basement rocks after 35 Ma (Figure 21) [*Luft et al.*, 2005]. Cosmogenic dating of pediment surfaces in the Namib Desert are consistent with late Neogene denudation and fluvial incision [*Van der Wateren and Dunai*, 2001]. It is likely that Neogene regional uplift has outpaced denudation across much of subequatorial Africa and does not have a clear thermochronologic signature [*Burke*, 1996; *Foster and Gleadow*, 1996; *Burke and Gunnell*, 2008; *Bauer et al.*, 2013].

4. Sediment Flux Histories

River channels and their tributaries are primary conduits for sedimentary transport. Thus, observations of sedimentary accumulation at major offshore deltas are a useful way of testing models that predict topographic growth as a function of time and space. *Milliman and Syvitski* [1992] analyzed the modern discharge of sediment from 280 rivers and concluded that sediment yield is strongly controlled by a combination

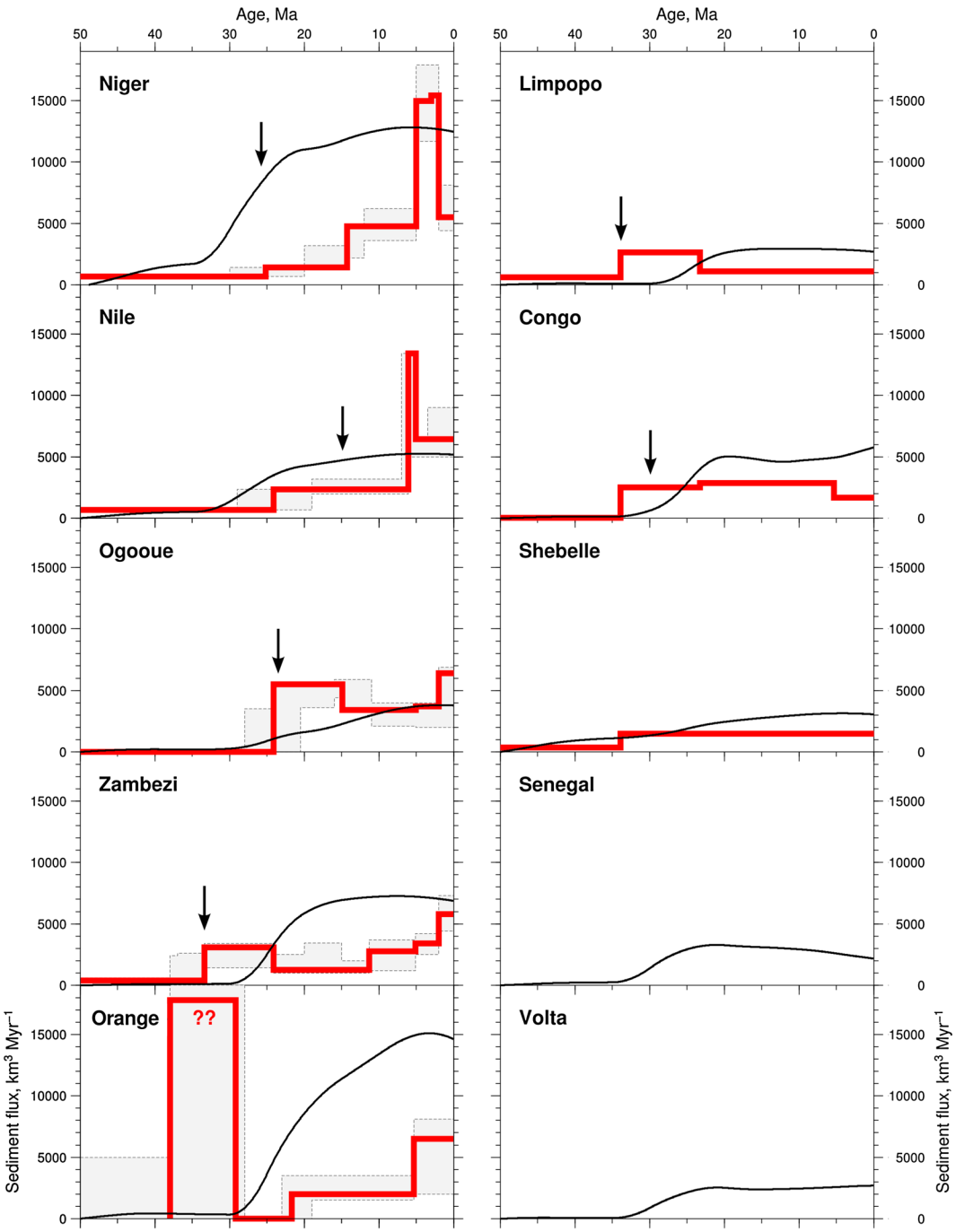

Figure 22. Observed and calculated solid sediment flux histories for 10 major catchments and their deltas (Figure 2a). Solid red lines and gray areas = offshore flux and uncertainty as function of time based upon on well logs and/or seismic reflection profiles [*Walford*, 2003] (Limpopo = *Dingle et al.* [1983]; Zambezi = *Walford et al.* [2005]; Shebelle = *DuToit et al.* [1997]; Nile = *Abdel Aal et al.* [2001] and *Hall et al.* [2005]). Black lines = flux histories calculated by modeling tributaries within catchment (see text); arrows = onset of clastic sedimentation. No data for Senegal and Volta deltas.

of basin size and relief. This global study was revised and expanded by *Milliman and Farnsworth* [2011] who analyzed 760 rivers for which sedimentary data exist. They confirmed that erosion, transport, and discharge of particulate and dissolved solids mostly reflect the cumulative effects of drainage basin size and morphology.

Here we scrutinize the relationship between observed and predicted sedimentary discharge for 10 African rivers. First, we devise a forward modeling technique to estimate the sediment flux of a drainage catchment

as a function of time. Given an uplift rate history, the shape of a river profile can be reconstructed with time. At any time, the area difference between a current and previous profile is a crude measure of the amount of eroded sediment at that time. A sediment flux history can be computed by integrating over differences between successive profiles for each time step. A similar scheme is used for different tributaries, thus enabling the total sediment flux for a drainage catchment as a function of time to be estimated. This flux is necessarily a minimum, but it can be adjusted using the difference between present-day topography and a summit envelope fitted to drainage divides.

Figure 22 shows preliminary estimates of predicted cumulative sedimentary flux for 10 African catchments. In each case, sediment flux dramatically increases between 30 and 20 Ma, coeval with the predicted growth of topography (Figure 15). Larger and steeper catchments (e.g., Niger, Orange, and Zambezi) produce much greater cumulative sediment fluxes than smaller and shallower catchments (Shebelle, Senegal, and Volta).

Despite significant uncertainties, it is illuminating to compare these predictions with measured estimates of solid sedimentary flux at major deltas. In the best constrained examples (e.g., Zambezi, Nile, and Orange), these estimates are based upon grids of regional seismic reflection profiles, which were calibrated with well-log information and used to map out the thickness and extent of sedimentary packages [e.g., *Walford et al.*, 2005; *Guillocheau et al.*, 2012; *Macgregor*, 2012]. In many deltas, clastic flux increases at 30 ± 5 Ma in agreement with predicted estimates. Total predicted volumes are highly smoothed overestimates since significant volumes of sediment can be transported into deeper waters. The largest differences between observed and predicted fluxes are for the Niger and Orange deltas. The Niger delta is deformed by thin-skinned extension and compression, which transports sedimentary packages downslope toward the base of the continental shelf where they are poorly imaged [*Cohen and McClay*, 1996; *Doust and Omatsola*, 1990]. Sedimentary bypass and longshore drift caused by the Benguela Current, which initiated during mid-Miocene times and intensified toward the present day, has dispersed sediment away from the Orange delta [*Rogers and Rau*, 2006; *Diester-Haass et al.*, 2002]. This dispersion is further complicated by changes of entry point of the Orange River between 28°S and 31°S up until late Miocene times [*Dingle and Hendey*, 1984].

There are other important discrepancies. For example, a rapid increase in sedimentation rate occurred between 5 and 10 Myr within the Niger, Nile, Ogooue, and Zambezi deltas. Rapid Plio-Pleistocene sedimentation of the Zambezi delta may be a consequence of capture of the upper Zambezi river, which previously drained into the Okavango delta, by the lower Zambezi river [*Walford et al.*, 2005].

Nonetheless, this preliminary analysis suggests that temporal and spatial patterns of regional uplift play an important role in determining sedimentary transport to large deltas. Peaks of sedimentation during Eocene, Miocene, and Pliocene times have been correlated with periods of maximum relief onshore [*Dollar*, 1998]. The existence of commonalities over large distances suggests that the driving mechanism operates over a regional scale, which is consistent with long-wavelength (greater than hundreds of kilometers) dynamic topographic support. Continent-scale climate change can also influence sediment budgets on short timescales [e.g., *Armitage et al.*, 2011; *Whittaker*, 2012]. Rapid changes of precipitation rate may not necessarily lead to sustained changes in sediment flux owing to negative feedback within the river catchment [*Armitage et al.*, 2011]. Temporal patterns of precipitation rate are generally short compared to the longevity of river profiles. It is likely that the effects of changing precipitation and sedimentary erodibility are subordinate to parameters such as basin area, elevation, and relief [*Milliman and Syvitski*, 1992; *Hovius*, 1998; *Milliman and Farnsworth*, 2011].

5. Discussion

The evolution of drainage networks is undoubtedly complicated and poorly understood. Despite lack of a proper dynamical description, modest progress can be made by analyzing large inventories of river profiles on a continent-wide basis. To carry out this analysis, we have developed an inverse algorithm that is based upon a widely used semiempirical description of river profile evolution. A fundamental premise is that the shape of a river profile is governed by uplift rate and moderated by erosive processes. Provided that these erosive processes can be adequately parameterized, it is possible to pose and solve the inverse problem, namely, what distribution of uplift rate as a function of space and time minimizes the misfit between observed and calculated river profiles?

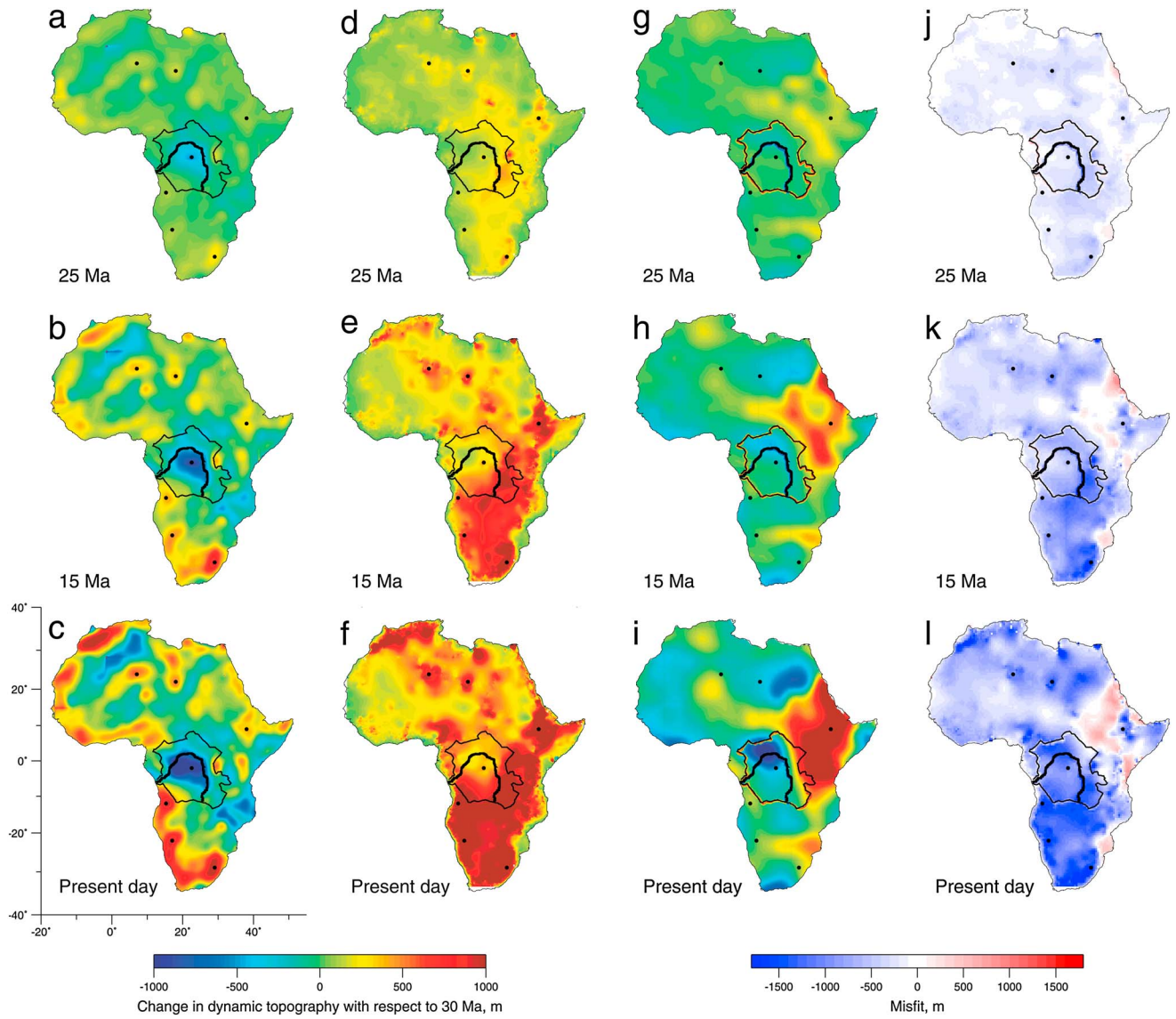

Figure 23. Dynamic topographic predictions. Black circles = loci of Hoggar, Tibesti, Afar, Congo, Bié, Namibian, and South African domes as reference aid. (a–c) Dynamic topography at 25, 15, and 0 Ma calculated from free-air gravity anomalies using admittance of 30 mGal km^{-1}. Note that growth of negative dynamic topography cannot be reliably reconstructed from river profiles. (d–f) Topography at 25, 15, and 0 Ma. (g–i) Dynamic topography calculated from seismic tomographic model using backward advection [*Moucha and Forte*, 2011]. (j–l) Difference between Figures 23d–23f and Figures 23g–23i.

Large numbers of river profiles on a continent-wide basis have been fitted with small residual misfits, and the predicted pattern of cumulative uplift through space and time broadly fits a suite of geologic and geophysical observations. The ability to model numerous river profiles in this way suggests that drainage networks are responding to external forcing. Uplift signals travel up river channels and their tributaries at speeds that depend nonlinearly on upstream drainage area. The coherency of these kinematic waves across multiple drainage catchments is striking and important.

These results suggest that African topography is youthful and that it developed over the last 30–40 Myr [*Burke*, 1996; *Burke and Gunnell*, 2008]. There have been other attempts to model African drainage patterns, which reached radically different conclusions. *Gilchrist et al.* [1994] carried out a series of numerical experiments which suggest that denudation of southwest Africa occurred before Cenozoic times. They suggested that the marginal topographic upwarps of Namibia and the western Cape were caused by flexural isostatic uplift, immediately following Mesozoic continental breakup. Forward models of landscape evolution, calibrated with fission track analyses, were used to support this hypothesis. *Van der Beek et al.* [2002] used a

similar approach to show that the Drakensberg Escarpment of southeast Africa was generated by Mesozoic continental breakup of Gondwanaland. Following a period of rapid fluvial incision, they suggested that the southern African margin has remained tectonically stable throughout Cenozoic times. Both arguments are based upon inferences made from numerical experiments of landscape development. *Gilchrist et al.* [1994] assume that their equivalent of κ is 5–10 $\times 10^3$ m^2 Ma^{-1} and that the fluvial transport coefficient multiplied by precipitation, $K_f v_R$, is 3–15 $\times 10^3$ m Ma^{-1}. *Van der Beek et al.* [2002] assume that κ is 10^3–10^4 m^2 Ma^{-1} and that $K_f v_R$ is 2–5 $\times$ 10^3 m Ma^{-1}. In both cases, their values of κ are smaller than 10^7 and can be disregarded. Since A is not explicitly included, their parameter $K_f v_R$ is equivalent to our advective coefficient, v, provided $m = 0$. If these values are compared, it is clear that *Gilchrist et al.* [1994] and *Van der Beek et al.* [2002] have run forward models that are 10 times too slow, which means that the Drakensberg Escarpment takes 100 Myr to retreat a distance of 100 km. According to the uplift rates determined from emergent marine terraces along the west and south African coastlines, $K_f v_R$ should actually be $>10^4$ m Ma^{-1}.

The relationship between topography and free-air gravity anomalies suggests that African physiography is maintained by the underlying pattern of mantle convection. *Gurnis et al.* [2000] and *Conrad and Gurnis* [2003] show that long-wavelength uplift of subequatorial Africa might be supported by a gigantic lower mantle convective anomaly. Neither model predicts the existence and growth of shorter-wavelength swells that rim southern Africa (Figure 23c). Instead, these swells may be supported by minor convective upwellings located immediately beneath the lithospheric plate [*Al-Hajri et al.*, 2010].

Moucha and Forte [2011] predict the development of African dynamic topography by simulating reverse advection of density anomalies identified from seismic tomographic models (Figures 23g–23i). Their model predicts growth and decay of short ($\sim 10^3$ km) wavelength basins and swells over the last 25 Myr. However, it is less successful at predicting the development of long-wavelength topography in subequatorial Africa (Figures 23j–23l). A dominant feature of their model is the Afar swell, which grows southward (Figure 23l). Shorter-wavelength swells (e.g., Hoggar, Tibesti, and Bié) and basins (e.g., Congo) are less well resolved.

The inability of dynamic models to predict detailed spatial and temporal patterns of cumulative uplift suggests that these features are supported by subplate convective anomalies that are, as yet, poorly resolved by global tomographic models. Regional surface wave tomographic models are capable of imaging some of these features (e.g., the Cameroon Line, the Hoggar, Tibesti, and Bié domes) [*Al-Hajri et al.*, 2010]. The sequential growth of shorter-wavelength African topography can be predicted by exploiting the interpretable signals contained within drainage networks.

6. Conclusions

We have modeled an inventory of 710 river profiles in order to reconstruct an uplift rate history for Africa since 50 Ma. The residual misfit between observed and predicted river profiles is 4.6. The cumulative uplift model suggests that African topography grew in two phases. Between 40 and 30 Ma, a series of small volcanic swells developed in North and East Africa. The largest of these swells occurred beneath Afar and quickly spread southwestward along the future East African Rift. At 20 Ma, long-wavelength uplift of subequatorial Africa commenced. Finally, a series of short-wavelength, and mostly amagmatic, swells grew along the Atlantic margin. This history is broadly consistent with a range of geomorphic, geologic, and geophysical constraints.

An inverse strategy enables us to investigate how erosional parameters affect our results. We conclude that shapes of river profiles are strongly controlled by knickzone retreat (i.e., detachment-limited advective processes) and that erosional diffusivity (i.e., transport-limited processes) plays a less significant role. Knickzone retreat is predominantly controlled by upstream drainage area to a fractional power (i.e., A^m where $m = 0.3$–0.5). Consequently, our results are not seriously affected by large variations in A (i.e., river capture events, drainage divide migration). There is no evidence for shock behavior (i.e., $n \sim 1$). Finally, we have used our strategy to investigate how precipitation rate changes affect calculated histories of uplift. We conclude that short-term (e.g., orbitally modulated) changes are unimportant but that systematic long-term (e.g., ~10 Myr) changes could affect predicted uplift rate histories.

King [1951] first articulated a link between multiple post-Gondwana erosion cycles and the development of pediplains and peneplains by parallel scarp retreat. He suggested that the succession of extensive flat surfaces which occur throughout southern Africa represents discrete episodes of landscape rejuvenation

[e.g., *King*, 1951; *Partridge and Maud*, 1987; *Burke and Gunnell*, 2008]. However, there is considerable debate about the veracity of this polycyclic landscape model. Alternative models suggest that peneplanation is lithologically controlled, emphasizing tectonic stability and negligible scarp retreat during Cenozoic times [*Gilchrist et al.*, 1994; *Brown et al.*, 2002; *Van der Beek et al.*, 2002]. Nevertheless, renewed axial uplift does appear to have occurred during Miocene and late Pliocene times and has been linked to the formation of a peneplained "post-African Surface," originally called the "African Surface" [*King*, 1951; *Burke and Gunnell*, 2008]. This uplift probably triggered deep incision along coastal reaches of southern African rivers. For example, the ~150 m deep Koa Valley was carved into basement rocks of Namaqualand 120 km from the coast [*Dollar*, 1998; *De Wit*, 1999]. During Pliocene times, straightening of lower reaches of the Orange River, generation of flights of aggradational fluvial terraces, and changes in river bed load to increasingly coarse clastic rocks, all reflect a pulse of regional uplift [*Dingle and Hendey*, 1984; *De Wit*, 1999; *Partridge and Maud*, 2000]. Others argue that drainage reorganization and subsequent landscape evolution are primarily controlled by Mesozoic rifting and marginal upwarp [*Gilchrist et al.*, 1994; *Van der Beek et al.*, 2002].

Our principal conclusion is that drainage networks contain interpretable signals about spatial and temporal patterns of regional uplift that sculpted the African landscape. Sequential growth of long- and short-wavelength swells suggests that different scales of convective circulation have operated beneath the African plate during Neogene times [*De Wit*, 2003; *Burke and Gunnell*, 2008]. One possibility is that a "superplume" is emplaced within the lower mantle, spawning localized upwellings within the upper mantle [*Nyblade and Robinson*, 1994; *Gurnis et al.*, 2000; *Lithgow-Bertelloni and Richards*, 1998]. Alternatively, spatial and temporal changes in lithospheric thickness could provide the dominant control for vertical motions. Either way, carefully calibrated modeling of drainage networks may provide a key to unlock the surficial manifestations of mantle processes.

Appendix A: Drainage Inventory

Table AI. Attributes of African Rivers From 10 Largest Drainage Basins (See Figures 13 and 14)

Name	Label	Longitude[a]	Latitude[b]	Elevation[c] (km)	Length (km)	Basin[d] ($km^2 \times 10^6$)
Congo Basin		12.38	−6.08			3.55
Aruwimi	AR			1.05	3100	
Bumba	BU			0.77	2220	
Chikapa	CK			0.57	2250	
Chinko	CH			0.61	2930	
Chiumbe	CE			1.14	2300	
CONGO	CO			1.33	4120	
Cuango	CG			1.10	2200	
Cuilo	CU			1.15	1680	
Doume	DO			0.66	2190	
Dja	DJ			0.66	2270	
Greiner	GR			1.51	4180	
Inzia	IN			1.03	1490	
Kadjema	KA			0.68	3190	
Kisantu	KS			0.94	610	
Kotto	KO			0.69	3000	
Kouango	KG			0.60	2410	
Kubudi	KB			0.80	4120	
Kundelungu	KU			1.27	4390	
Kwilu	KW			1.07	1620	
Liridi	LD			0.75	2880	
Lobaye	LB			0.76	2160	
Lokoro	LR			0.34	1270	
Lomami	LO			0.97	3760	
Lomelai	LJ			0.57	2230	
Lopori	LP			0.56	2030	

Table AI. (continued)

Name	Label	Longitude[a]	Latitude[b]	Elevation[c] (km)	Length (km)	Basin[d] ($km^2 \times 10^6$)
Loto	LT			0.74	4450	
Lowa	LW			1.52	3050	
Lua	LX			0.39	1960	
Luama	LM			1.49	3370	
Lufira	LF			1.36	4060	
Lufunzo	LN			1.26	3960	
Lui	LI			1.27	2100	
Luilaka	LA			0.48	1930	
Luizi (east)	LZ			1.75	3890	
Luizi (west)	LY			1.93	4080	
Lukenje	LE			0.44	1770	
Lukuga	LU			1.29	4120	
Lukulu	LK			1.76	3070	
Lulua	LL			0.99	2460	
Lushiko	LS			1.17	2030	
Luvua	LV			1.56	3950	
Mambili	MA			0.41	1470	
Maringa	MR			0.48	2030	
Mohemba	MM			1.35	3820	
Mongala	MO			0.48	2050	
Motaba	MT			0.58	1720	
M'Pama	MP			0.57	1370	
Nepoko	NE			1.20	2840	
Niemba	NI			1.36	4100	
Oubangui	OU			1.16	3660	
Sankuru	SA			0.96	2450	
Tele	TE			0.63	2440	
Tshuapa	TS			0.45	2270	
Limpopo Basin		33.52	−25.20			0.39
Letaba	LE			0.51	540	
LIMPOPO	LI			1.68	1660	
Lotsani	LO			1.28	1200	
Maklautsi	MA			1.18	1200	
Messina	ME			1.34	920	
Olifanta	OL			1.55	1050	
Ramaselwana	RA			1.09	1350	
Shashe	SH			1.32	1150	
Niger Basin		5.97	4.34			2.12
Agadem	AG			0.46	3010	
Amachkalo	AM			0.94	2830	
Anderboulane	AN			0.44	2080	
Aouana	AO			0.34	4180	
Ati Batha	AB			0.62	2970	
Azaouak	AZ			1.95	3480	
Bahr Azoum	BZ			0.53	2990	
Bahrel Ghazal	BG			2.44	3450	
Bahr Sara	BA			0.53	2700	
Baminghi	BM			0.48	2550	
Bankor	BK			0.32	3790	
Bani	BN			0.41	3900	
Batha	BT			0.53	2610	
Benoué	BE			1.13	1600	
Bounag	BO			0.37	3610	
Diaka	DI			0.31	3000	
Dogota	DO			0.62	4120	

Table AI. (continued)

Name	Label	Longitude[a]	Latitude[b]	Elevation[c] (km)	Length (km)	Basin[d] ($km^2 \times 10^6$)
Donga	DA			1.28	1100	
Faguibine	FA			0.38	3420	
Fazei	FZ			1.11	3560	
Gindi	GI			0.61	1740	
Gongola	GO			1.29	1730	
Gouri	GR			1.70	4020	
Gulbi Rima	GU			0.54	2140	
Igadiane	IG			1.22	2880	
Isazagene	IS			0.55	2950	
Kabga	KB			1.00	3840	
Kaduna	KA			0.70	1030	
Kharma	KH			0.82	4030	
Komadugu Yobé	KO			0.57	2720	
Kouaro	KU			0.47	3480	
Logone	LO			1.03	2300	
Maouri	MI			0.45	1940	
N'Gourn	NG			0.35	2190	
NIGER	NI			0.93	4000	
Nkaola	NK			0.71	4260	
Oulata	OU			0.32	2980	
Ras el Ma	RM			0.35	2890	
Rime	RI			0.93	2710	
Salamat	SA			1.19	3820	
Sirba	SI			0.31	1920	
Sokoto	SO			0.49	1980	
Tafassasset	TA			1.69	4320	
Tamandouriri	TM			0.40	4470	
Tapo	TP			0.37	1630	
Tasr	TS			0.52	2560	
Tilemsi	TI			0.84	2840	
Tinguesefen	TN			0.47	2600	
Uahm	UA			0.89	2900	
Ude	UD			1.04	3720	
Yat	YT			0.81	3720	
Yatakalu	YA			0.28	2190	
Yumbum	YB			0.57	2720	
Zagarat	ZA			0.61	2560	
Zouar	ZO			1.38	3930	
Nile Basin		31.20	31.56			3.78
Adda	AD			0.67	5240	
Akobo	AK			2.34	5840	
Amair	AM			0.84	3360	
Amur	AR			0.56	2190	
Angareo	AN			2.14	3820	
Assua	AS			1.18	6010	
Atbara	AT			3.42	4210	
Ayod	AY			0.42	4420	
Bahr el Arab	BA			0.77	5490	
Bar	BR			1.10	3140	
Baro	BO			1.77	4780	
Dinder	DI			0.78	4130	
Dongola	DO			0.60	2470	
Gabgaba	GA			0.51	1930	
Gabra	GB			0.65	5180	
Hawar	HA			0.92	3630	

Table AI. (continued)

Name	Label	Longitude[a]	Latitude[b]	Elevation[c] (km)	Length (km)	Basin[d] ($km^2 \times 10^6$)
Ibra	IB			0.93	5540	
Jur	JU			0.62	5140	
Kapoeta	KP			1.13	5260	
Kitgum	KI			1.06	5370	
Kodok	KD			0.60	4210	
Kurkur	KK			0.47	2130	
Kuror	KX			0.62	2730	
Kurru	KU			0.86	4660	
Lao	LA			0.78	4880	
Lol	LO			0.77	5060	
Magaddam	MA			0.41	2680	
Manyonga	MY			1.17	6680	
Mara	MR			2.04	6070	
Medu	MU			0.90	3270	
Melik	ME			0.59	2940	
Milani	MI			0.77	2690	
Mubende	MB			1.26	6130	
NILE (Albert)	NA			1.58	6650	
Nile (Blue)	NB			2.92	5110	
Nile (Victoria)	NV			1.51	6750	
Numatuing	NU			0.66	5070	
Nyama	NY			0.69	4200	
Nzoya	NZ			1.95	6120	
Oena	OE			0.65	1150	
Orangi	OR			1.87	6310	
Pibor	PI			1.06	5160	
Rahat	RH			0.54	3610	
Rumeila	RU			0.47	3220	
Sageig	SA			0.53	3620	
Setima	SE			0.37	2160	
Shaiyt	SH			0.43	1400	
Shawa	SW			1.11	4270	
Simiyu	SY			1.70	6390	
Sobat	SO			2.43	5710	
Sunte	SU			0.72	2900	
Tendik	TE			0.59	4120	
Tori	TO			1.33	4920	
Toshka	TX			0.67	2540	
Yei	YE			0.87	5040	
Ogooue Basin		8.91	−1.06			0.20
Abanga	AB			0.57	520	
Djaddie	DJ			0.57	920	
Ivina	IV			0.61	1020	
Lolo	LO			0.87	810	
Muniangui	MU			0.56	770	
M'Vung	MV			0.50	710	
N'Gourmie	NG			0.72	670	
Ofoué	OF			0.88	670	
OGOOUE	OG			0.57	990	
Sébé	SE			0.60	930	
Orange Basin		18.19	-31.70			0.92
Auob	AU			2.03	1810	
Brak	BR			1.56	1500	
Caledon	CA			1.97	2230	
Fish	FI			1.31	1030	

Table AI. (continued)

Name	Label	Longitude[a]	Latitude[b]	Elevation[c] (km)	Length (km)	Basin[d] ($km^2 \times 10^6$)
Genesa	GE			1.45	1420	
Hartbees	HS			1.73	1480	
Harts	HA			1.52	1910	
Hohewarte	HH			1.62	1690	
Karas	KA			1.05	670	
Kenhardt	KE			1.43	1130	
Konkiep	KO			1.67	620	
Kuruman	KU			1.29	1280	
Mashowing	MA			1.58	1440	
Molopo	MO			1.54	1930	
Nossob	NO			1.81	2020	
Oikhe	OI			1.18	1480	
Okha	OK			1.24	1880	
ORANGE	OR			3.04	2460	
Riet	RI			1.59	1790	
Sandfontein	SA			1.28	1550	
Ukamas	UK			1.54	800	
Vaal	VA			1.75	2600	
Vaisch	VI			1.65	2140	
Vet	VT			1.52	2000	
Vrede	VR			1.78	2450	
Senegal Basin		−16.50	16.04			0.69
Bafing	BA			0.52	1430	
Dalaba	DA			0.50	1520	
Falémé	FA			0.73	1810	
Ferlo	FE			0.08	730	
Gorgol (Black)	GB			0.40	1520	
Gorgol (White)	GO			0.62	1510	
Karakoro	KA			0.24	1400	
Kolimbiné	KO			0.44	2150	
Koniakary	KK			0.30	1400	
Ouasan	OU			0.14	800	
Nioro	NI			0.28	1990	
Rkiz	RK			0.34	1010	
SENEGAL	SE			0.43	2030	
Shebelle Basin		42.63	−0.25			0.75
Baidoa	BA			0.71	960	
Errer	ER			2.06	1980	
Ewaso Ng'iro	EW			4.28	1180	
Fafen	FA			2.53	1920	
Jubba (Dawo)	JD			1.52	1530	
Jubba (Genale)	JG			4.11	1470	
Jubba (Webi)	JW			4.08	1610	
Kgherta	KG			0.48	660	
Kutulo	KU			1.86	1090	
Lak Bor	LA			1.78	1090	
Milgis	MI			1.97	1360	
Missarole	MI			0.50	970	
SHEBELLE	SH			2.67	2350	
Web	WB			0.56	1020	
Volta Basin		0.67	5.77			0.38
Boumfum	BO			0.25	390	
Diebougou	DI			0.43	1790	
Oti	OT			0.59	1380	
Pama	PA			0.29	1170	

Table AI. (continued)

Name	Label	Longitude[a]	Latitude[b]	Elevation[c] (km)	Length (km)	Basin[d] ($km^2 \times 10^6$)
VOLTA (Black)	VB			0.33	1840	
Volta (Red)	VR			0.32	1300	
Volta (White)	VW			0.34	1640	
Yagaba	YA			0.31	1120	
Yendi	YE			0.24	780	
Zambezi Basin		36.29	−18.86			1.95
Botlete	BO			1.17	2890	
Cuando	CO			1.29	3030	
Cubango	CU			1.42	3240	
Cuito	CT			1.35	3280	
Domba	DA			1.51	3100	
Dowa	DO			1.25	1220	
Duenga	DU			1.37	1540	
Eiseb	EI			1.23	2780	
Epukiro	EP			1.62	2840	
Garu	GA			1.18	2730	
Gwaai	GW			1.29	1900	
Hunyani (east)	HU			1.64	1360	
Hunyani (west)	HY			1.53	1340	
Kabompo	KA			1.29	2960	
Kafue	KF			1.43	2400	
Kalomo	KO			1.31	1690	
Luancundu	LN			1.24	2650	
Luanginga	LI			1.45	2750	
Luangwa	LG			1.38	1960	
Luena	LE			1.19	2980	
Lumuna	LM			1.18	2600	
Lunga (east)	LX			1.43	2960	
Lunga (west)	LA			1.49	2210	
Lungwebungu	LU			1.31	3120	
Lunsemfwa	LF			1.47	1410	
Mashewa	MA			1.19	2750	
Mochabe	ME			1.46	2750	
Mozoe	MO			1.65	910	
Mpatane	MP			1.09	2470	
Muangadeze	MG			0.97	840	
Mulungushi	MU			1.19	1330	
Munyati	MY			1.55	1750	
Oikhe	OH			1.15	2790	
Okaua	OU			1.54	2780	
Okavango	OK			1.76	3500	
Revugo	RE			1.44	780	
Rietfontein	RI			1.52	3160	
Ruo	RU			1.34	1610	
Sengwa	SA			1.07	1470	
Seramounta	SE			1.12	1980	
Serowe	SW			1.21	2540	
ZAMBEZI	ZA			1.17	2960	

[a]Longitude of river mouth in decimal degrees.
[b]Latitude of river mouth in decimal degrees.
[c]Maximum elevation.
[d]Area of drainage basin calculated from SRTM data set.

Notation

z elevation of river (L)
L river length (L)
x distance (L)
y distance (L)
A upstream drainage area (L^2)
t time (T)
τ_G Gilbert time (T)
U uplift rate ($L\ T^{-1}$)
L erosion rate ($L\ T^{-1}$)
v advective coefficient of erosion ($L^{1-2m}\ T^{-1}$)
m area exponent
n slope exponent
κ diffusive coefficient of erosion ($L^2\ T^{-1}$)
$X \times Y$ number of spatial dimensions
T number of temporal dimensions
M number of rivers
N number of data points along each river
f positivity constraint
S precipitation constant
μ Lagrangian multiplier
Q discharge ($L^3\ T^{-1}$)
p precipitation rate ($L\ T^{-1}$)

Acknowledgments
J.D.P. and G.G.R. were supported by the BP-Cambridge Margins Project. We thank A. Bump, R. Corfield, A. Crosby, M. Daly, J. Hossack, L. Mackay, M. Thompson, and J. Winterbourne for their help and encouragement. Figures were prepared using Inkscape and GMT4.2.0. Department of Earth Sciences contribution esc.3032.

References

Abdel Aal, A., A. El Barkooky, M. Gerrits, H. Meyer, M. Schwander, and H. Zaki (2001), Tectonic evolution of the Eastern Mediterranean Basin and its significance for the hydrocarbon prospectivity of the Nile Delta deepwater area, *GeoArabia*, *6*, 363–384.
Al-Hajri, Y., N. White, and S. Fishwick (2010), Scales of transient convective support beneath Africa, *Geology*, *37*(10), 883–886.
Anka, Z., and M. Séranne (2004), Reconnaissance study of the ancient Zaire (Congo) deep-sea fan (ZaiAngo Project), *Mar. Geol.*, *209*, 223–244.
Armitage, A., R. Duller, A. Whittaker, and P. Allen (2011), Transformation of tectonic and climatic signals from source to sedimentary archive, *Nat. Geosci.*, *4*, 231–235.
Bauer, F., U. Glasmacher, U. Ring, M. Karl, A. Schumann, and B. Nagudi (2013), Tracing the exhumation history of the Rwenzori Mountains, Albertine Rift, Uganda, using low-temperature thermochronology, *Tectonophysics*, *599*, 8–28.
Beccaluva, L., G. Bianchini, R. Ellam, C. Natali, A. Santato, F. Siena, and F. Stuart (2011), Peridotite xenoliths from Ethiopia: Inferences about mantle processes from plume to rift settings, *Geol. Soc. Am. S.*, *478*, 77–104.
Bond, G. (1978), Evidence for Late Tertiary uplift of Africa relative to North America, South America, Australia and Europe, *J. Geol.*, *86*(1), 47–65.
Brocard, G., and P. van der Beek (2006), Influence of incision rate, rock strength, and bedload supply on bedrock river gradients and valley-flat widths: Field-based evidence and calibrations from western Alpine rivers (southeast France), *Geol. Soc. Am. Spec. Pap.*, *398*, 101–126.
Brown, R., M. Summerfield, and A. Gleadow (2002), Denudational history along a transect across the Drakensberg Escarpment of southern Africa derived from apatite fission track thermochronology, *J. Geophys. Res.*, *107*(B12), 2350, doi:10.1029/2001JB000745.
Burke, K (1996), The African plate, *S. Afr. J. Geol.*, *99*, 339–410.
Burke, K., and Y. Gunnell (2008), *The African Erosion Surface: A Continental-Scale Synthesis of Geomorphology, Tectonics, and Environmental Change Over the Past 180 Million Years*, vol. 201, 1–66.
Chang, S.-J., and S. Van der Lee (2011), Mantle plumes and associated flow beneath Arabia and East Africa, *Earth Planet. Sci. Lett.*, *302*, 448–454.
Choubert, G., and A. Faure-Muret (1976), *Geological World Atlas*, Int. Geol. Map. Bur., UNESCO, Paris.
Cohen, H., and K. McClay (1996), Sedimentation and shale tectonics of the northwestern Niger Delta front, *Mar. Pet. Geol.*, *13*, 313–328.
Conrad, C., and M. Gurnis (2003), Seismic tomography, surface uplift, and the breakup of Gondwanaland: Integrating mantle convection backwards in time, *Geochem. Geophys. Geosyst.*, *4*(3), 1031, doi:10.1029/2001GC000299.
Cook, K., K. Whipple, A. Heimsath, and T. Hanks (2009), Rapid incision of the Colorado River in Glen Canyon—Insights from channel profiles, local incision rates, and modeling of lithologic controls, *Earth Surf. Processes Landforms*, *34*, 994–1010.
Cox, K. (1989), The role of mantle plumes in the development of continental drainage patterns, *Nature*, *342*, 873–877.
Crosby, A., S. Fishwick, and N. White (2010), Structure and evolution of the intracratonic Congo Basin, *Geochem. Geophys. Geosyst.*, *11*, Q06010, doi:10.1029/2009GC003014.
De Wit, M. (1999), Post-Gondwana drainage and the development of diamond placers in western South Africa, *Econ. Geol.*, *94*, 721–740.
De Wit, M. (2003), Madagascar: Heads it's a continent, tails it's an island, *Annu. Rev. Earth Planet. Sci.*, *31*, 213–248.
Diester-Haass, L., P. Meyers, and L. Vidal (2002), The late Miocene onset of high productivity in the Benguela Current upwelling system as part of a global pattern, *Mar. Geol.*, *180*(1-4), 87–103.
Dingle, R., and Q. Hendey (1984), Late Mesozoic and Tertiary sediment supply to the Eastern Cape Basin (SE Atlantic) and palaeo-drainage systems in southwestern Africa, *Mar. Geol.*, *56*, 13–26.
Dingle, R., W. Seisser, and A. Newton (1983), *Mesozoic and Tertiary Geology of Southern Africa*, Balkema, Rotterdam.

Divins, D. (2008), *NGDC Total Sediment Thickness of the World's Oceans & Marginal Seas*. [Retrieved from http://ngdc.noaa.gov/mgg/sedthick/sedthick.html.]
Dollar, E. (1998), Paleofluvial geomorphology in southern Africa: A review, *Prog. Phys. Geog.*, *22*(3), 325–349.
Doust, H., and E. Omatsola (1990), Niger Delta, *AAPG Bulletin*, *48*, 201–238.
Dugda, M., A. Nyblade, J. Julia, C. Langston, C. Ammon, and S. Simiyu (2005), Crustal structure in Ethiopia and Kenya from receiver function analysis: Implications for rift development in Eastern Africa, *J. Geophys. Res.*, *110*, doi:10.1029/2004JB003065.
DuToit, S., A. Kidston, and O. Slind (1997), *The Hydrocarbon Potential of the East Africa Continental Margin*, Alconsult International Ltd, Toronto, Canada.
Ebinger, C., and N. Sleep (1998), Cenozoic magmatism throughout East Africa resulting from impact of a single plume, *Nature*, *395*, 788–791.
Ebinger, C., A. Deino, R. Drake, and A. Tesha (1989), Chronology of volcanism and rift basin propagation: Rungwe volcanic province, East Africa, *J. Geophys. Res.*, *94*, 15,785–15,803.
Elmejdoub, N., and Y. Jedoui (2009), Pleistocene raised marine deposits of the Cap Bon peninsula (N-E Tunisia): Records of sea-level highstands, climatic changes, and coastal uplift, *Geomorphology*, *112*, 179–189.
Farr, T., et al. (2007), The Shuttle Radar Topographic Mission, *Rev. Geophys.*, *45*, RG2004, doi:10.1029/2005RG000183.
Feakins, S., and P. Demenocal (2008), Global and African Regional Climate during the Cenozoic, in *Cenozoic Mammals of Africa*, edited by L. Werdelin and B. Sanders, pp. 45–55, Univ. of Calif. Press, Berkeley.
Fishwick, S., and I. Bastow (2011), Towards a better understanding of African topography, a review of passive-source seismic studies of the African crust and upper mantle, in *The Formation and Evolution of Africa: A Synopsis of 3.8 Ga of Earth History*, edited by D. J. J. Van Hinsbergen et al., *Geol. Soc. London Spec. Publ.*, 357, 343–371.
Flowers, R., and B. Schoene (2010), (U-Th)/He thermochronometry constraints on unroofing of the Eastern Kaapvaal craton and significance for uplift of the Southern African Plateau, *Geology*, *38*(9), 827–830.
Forte, A., S. Quéré, R. Moucha, N. Simmons, S. Grand, J. Mitrovica, and D. Rowley (2010), Joint seismic-geodynamic-mineral physical modelling of African geodynamics: A reconciliation of deep-mantle convection with surface geophysical constraints, *Earth Planet. Sci. Lett.*, *295*, 329–241.
Foster, D., and A. Gleadow (1996), Structural framework and denudation history of the flanks of the Kenya and Anza Rifts, East Africa, *Tectonics*, *15*(2), 258–271.
Frierson, D., J. Lu, and G. Chen (2007), Width of the Hadley cell in simple and comprehensive general circulation models, *Geophys. Res. Lett.*, *34*, L18804, doi:10.1029/2007GL031115.
Furman, T., J. Bryce, T. Rooney, B. Hana, G. Yirgu, and D. Ayalew (2006), Heads and tails: 30 million years of the Afar plume, in *The Afar Volcanic Province Within the East African Rift System*, edited by G. Yirgu, C. J. Ebinger, and P. K. H. Maguire, *Geol. Soc. London Spec. Publ., 259*, 95–119.
Gani, N., M. Gani, and M. Abdelsalam (2007), Blue Nile incision on the Ethiopian Plateau: Pulsed plateau growth, Pliocene uplift, and hominin evolution, *GSA Today*, *17*, 4–11.
George, R., and N. Rogers (2002), Plume dynamics beneath the African plate inferred from the geochemistry of the Tertiary basalts of southern Ethiopia, *Contrib. Mineral. Petrol.*, *144*(3), 286–304.
Gilchrist, A., H. Kooi, and C. Beaumont (1994), Post-Gondwana geomorphic evolution of southwestern Africa: Implications for the controls on landscape development from observations and numerical experiments, *J. Geophys. Res.*, *99*(B6), 12,211–12,228.
Goudarzi, G. (1970), *Geology and Mineral Resources of Libya: A Reconnaissance, U. S. Geol. Surv. Prof. Pap., 660,* 104 pp.
Guillocheau, F., D. Rouby, C. Robin, C. Helm, N. Rolland, C. Le Carier de Veslud, and J. Braun (2012), Quantification and causes of the terrigenous sediment budget at the scale of a continental margin: A new method applied to the Namibia-South Africa margin, *Basin Res.*, *24*, 3–30.
Guiraud, M., A. Buta-Neto, and D. Quesne (2010), Segmentation and differential post-rift uplift at the Angola margin as recorded by the transform-rifted Benguela and oblique-to-orthogonal-rifted Kwanza basins, *Mar. Pet. Geol.*, *27*, 1040–1068.
Gurnis, M., J. Mitrovica, J. Ritsema, and H.-J van Heijst (2000), Constraining mantle density structure using geological evidence of surface uplift rates: The case of the African Superplume, *Geochem. Geophys. Geosyst.*, *1*(7), 1020, doi:10.1029/1999GC000035.
Hack, J. (1957), Studies of longitudinal stream profiles in Virginia and Maryland, *U. S. Geol. Surv. Prof. Pap., 294B*, 45–80.
Hall, J., V. Krashenninkov, F. Hirsch, C. Benjamini, and A. Flexer (2005), *Geological Framework of the Levant, Volume II: The Levantine Basin and Israel*, Historical Productions, Jerusalem.
Hansen, S., A. Nyblade, and M. Benoit (2012), Mantle structure beneath Africa and Arabia from adaptively parameterized P-wave tomography: Implications for the origin of Cenozoic Afro-Arabian tectonism, *Earth Planet. Sci. Lett.*, *319*, 23–34.
Holmes, A. (1944), *Principles of Physical Geology*, London and Edinburgh.
Hovius, N. (1998), Controls on sediment supply by large rivers, in *Relative role of Eustasy, Climate and Tectonism in Continental Rocks*, edited by K. W. Shanley and P. J. McCabe, *SEPM Spec. Publ., 59*, 3–16.
Ismail, A., M. Boukhary, and A. Abdel Naby (2010), Subsurface stratigraphy and micropaleontology of the Neogene rocks, Nile Delta, Egypt, *Geol. Croat.*, *63*(1), 1–26.
Jackson, M., M. Hudec, and K. Hegarty (2005), The Great West African Tertiary coastal uplift: Fact or fiction? A perspective from the Angolan divergent margin, *Tectonics*, *24*, TC6014, doi:10.1029/2005TC001836.
Jacobs, B., and P. Herendeen (2004), Eocene dry climate and woodland vegetation in tropical Africa reconstructed from fossil leaves from northern Tanzania, *Palaeogeogr. Palaeoclimatol. Palaeoecol.*, *213*, 115–123.
Jones, S. M., B. Lovell, and A. G. Crosby (2012), Comparison and modern and geological observations of dynamic support from mantle convection, *J. Geol. Soc. London*, *169*, 745–758, doi:10.1144/jgs2011-118.
King, L. (1951), *South African Scenery,* 2nd ed., Oliver and Boyd, Edinburgh, U. K.
Kirby, E., K. Whipple, W. Tang, and Z. Chen (2003), Distribution of active rock uplift along the eastern margin of the Tibetan Plateau: Inferences from bedrock channel longitudinal profiles, *J. Geophys. Res.*, *108*(B4), 2217, doi:10.1029/2001JB000861.
Kröpelin, S., and I. Soulié-Märsche (1991), Charophyte remains from Wadi Howar as evidence for deep mid-Holocene freshwater lakes in the eastern Sahara of northwest Sudan, *Quat. Res.*, *36*, 210–223.
Lavier, L., M. Steckler, and F. Brigaud (2001), Climatic and tectonic controls on the Cenozoic evolution of the West African continental margin, *Mar. Geol.*, *178*, 63–80.
Liégeois, J.-P., A. Benhallou, A. Azzouni-Sekkal, R. Yahiaoui, and B. Bonin (2005), The Hoggar swell and volcanism: Reactivation of the Precambrian Tuareg Shield during Alpine convergence and West African Cenozoic volcanism, in *Plates, Plumes, and Paradigms*, edited by G. R. Foulger et al., *Geol. Soc. Am. Spec. Pap., 388*, 379–400.
Lithgow-Bertelloni, C., and M. Richards (1998), The dynamics of Cenozoic and Mesozoic plate motions, *Rev. Geophys.*, *36*(1), 27–8.

Luft, F., J. Chemale, V. Lelarge, and J. Avila (2005), Post-Gondwana break-up record constraints from apatite fission track thermochronology in NW Namibia, *Radiat. Meas.*, *39*, 675–679.
Macgregor, D. (2012), The Cameroon Volcanic Line revisited: Petrogenesis of continental basaltic magmas from lithospheric and asthenospheric mantle sources., *Pet. Geosci.*, *18*(4), 417–431.
McDougall, I., and F. Brown (2009), Timing of volcanism and evolution of the Northern Kenya Rift, *Geol. Mag.*, *146*, 34–47.
McKenzie, D., and D. Fairhead (1997), Estimates of the effective elastic thickness of the continental lithosphere from Bouguer and free air gravity anomalies, *J. Geophys. Res.*, *102*(B12), 27,523–27,552.
McKenzie, D., and K. Priestley (2008), The influence of lithospheric thickness variations on continental evolution, *Lithos*, *102*, 1–11.
Milliman, J., and K. Farnsworth (2011), *River Discharge to the Coastal Ocean: A Global Synthesis*, Cambridge Univ. Press, Cambridge.
Milliman, J., and J. Syvitski (1992), Geomorphic/tectonic control of sediment discharge to the ocean: The importance of small mountainous rivers, *J. Geol.*, *100*, 525–544.
Moucha, R., and A. M. Forte (2011), Changes in African topography driven by mantle convection, *Nat. Geosci.*, *4*(10), 707–712.
Nair, S., S. Gao, K. Liu, and P. Silver (2006), Southern African crustal evolution and composition: Constraints from receiver function studies, *J. Geophys. Res.*, *111*, B02304, doi:10.1029/2005JB003802.
Ni, S., E. Tan, K. Liu, and P. Silver (2002), Sharp sides to the African superplume, *Science*, *296*, 1850–1852.
Nicholson, S. (2001), Climatic and environmental change in Africa during the last two centuries, *Clim. Res.*, *17*, 123–144.
Nyagah, K. (1995), Stratigraphy, depositional history and environments of deposition of Cretaceous through Tertiary strata in the Lamu Basin, southeast Kenya and implications for reservoirs for hydrocarbon exploration, *Sediment. Geol.*, *96*, 43–71.
Nyblade, A., and S. Robinson (1994), The African superswell, *Geophys. Res. Lett.*, *21*, 765–768.
Odada, E. (1996), Geological evolution of coastal Kenya as inferred from sedimentary sequences and marine terraces, *Afr. Geosci. Rev.*, *3*(3), 1–18.
Parker, R. (1994), *Geophysical Inverse Theory*, 386 pp., Princeton Univ. Press, Princeton, New Jersey.
Parrish, J., and R. Curtis (1982), Atmospheric circulation, upwelling, and organic-rich rock in the Mesozoic and Cenozoic eras, *Palaeogeogr. Palaeoclimatol. Palaeoecol.*, *40*, 31–66.
Partridge, T. (1998), Of diamonds, dinosaurs and diastrophism: 150 Myr of landscape evolution in Southern Africa, *S. Afr. J. Geol.*, *101*, 167–184.
Partridge, T., and R. Maud (1987), Geomorphic evolution of southern Africa since the Mesozoic, *S. Afr. J. Geol.*, *90*, 167–184.
Partridge, T., and R. Maud (Eds.) (2000), *The Cenozoic of Southern Africa*, Oxford Univ. Press, New York.
Permenter, J., and C. Oppenheimer (2007), Volcanoes of the Tibesti Massif (Chad, northern Africa), *Bull. Volcanol.*, *69*, 609–626.
Press, W. H., S. A. Teukolsky, W. T. Vetterling, and B. Flannery (1992), *Numerical Recipes in Fortran: The Art of Scientific Computing,* 2nd ed., Cambridge Univ. Press, Cambridge, U. K.
Priestley, K., and D. McKenzie (2006), The thermal structure of the lithosphere from shear wave velocities, *Earth Planet. Sci. Lett.*, *244*, 285–301.
Priestley, K. F., D. P. McKenzie, E. Debayle, and S. Pilidou (2009), The African upper mantle and its relationship to tectonics and surface geology, *Geophys. J. Int.*, *175*(3), 1108–1126.
Pritchard, D., G. Roberts, N. White, and C. Richardson (2009), Uplift histories from river profiles, *Geophys. Res. Lett.*, *36*, L24301, doi:10.1029/2009GL040928.
Raab, M., R. Brown, K. Gallagher, A. Carter, and K. Weber (2002), Late Cretaceous reactivation of major crustal shear zones in northern Namibia: Constraints from apatite fission track analysis, *Tectonophysics*, *349*, 75–92.
Raab, M., R. Brown, K. Gallagher, K. Weber, and A. Gleadow (2005), Denudational and thermal history of the Early Cretaceous Brandberg and Okenyenya igneous complexes on Namibia's Atlantic passive margin, *Tectonics*, *24*, TC3006, doi:10.1029/2004TC001688.
Reid, D., A. Cooper, D. Rex, and R. Harmer (1990), Timing of post-Karoo alkaline volcanism in southern Namibia, *Geol. Mag.*, *5*, 427–433.
Reijers, T. (2011), Stratigraphy and sedimentology of the Niger Delta, *Geologos*, *17*(3), 133–162.
Ritsema, J., A. Deuss, H. J. van Heijst, and J. H. Woodhouse (2011), S40RTS: A degree-40 shear-velocity model for the mantle from new Rayleigh wave dispersion, teleseismic traveltime and normal-mode splitting function measurements, *Geophys. J. Int.*, *184*(3), 1223–236.
Roberts, D., and J. Brink (2002), Dating and correlation of Neogene coastal deposits in the Western Cape (South Africa): Implications for Neotectonism, *S. Afr. J. Geol.*, *105*, 337–352.
Roberts, G., and N. White (2010), Estimating uplift rate histories from river profiles using African examples, *J. Geophys. Res.*, *115*, B02406, doi:10.1029/2009JB006692.
Roberts, G., J. Paul, N. White, and J. Winterbourne (2012a), Temporal and spatial evolution of dynamic support from river profiles: A framework for Madagascar, *Geochem. Geophys. Geosyst.*, *13*, Q04004, doi:10.1029/2012GC004040.
Roberts, G., N. White, G. Martin-Brandis, and A. Crosby (2012b), An uplift history of the Colorado Plateau and its surroundings from inverse modeling of longitudinal river profiles, *Tectonics*, *31*, doi:10.1029/2012TC003107.
Roe, G., D. Montgomery, and B. Hallet (2002), Effects of orographic precipitation variations on the concavity of steady-state river profiles, *Geology*, *30*, 143–146.
Rogers, J., and A. Rau (2006), Surficial sediments of the wave-dominated Orange River Delta and the adjacent continental margin off south-western Africa, *Afr. J. Mar. Sci.*, *28*(3–4), 511–524.
Rosenbloom, N., and R. Anderson (1994), Hillslope and channel evolution in a marine terraced landscape, Santa Cruz, California, *J. Geophys. Res.*, *99*(B7), 14,013–14,029.
Royden, L., and J. Perron (2013), Solutions of the stream power equation and application to the evolution of river longitudinal profiles, *J. Geophys. Res. Earth Surf.*, *118*, 497–518.
Sahagian, D. (1988), Epeirogenic motions of Africa as inferred from Cretaceous shoreline deposits, *Tectonics*, *7*(1), 125–138.
Salman, G., and I. Abdula (1995), Development of the Mozambique and Ruvuma sedimentary basins, offshore Mozambique, *Sediment. Geol.*, *96*, 7–41.
Schoenbohn, L., K. Whipple, B. Burchfiel, and L. Chen (2004), Geomorphic constraints on surface uplift, exhumation, and plateau growth in the Red River region, Yunnan Province, China, *Geol. Soc. Am. Bull.*, *116*(7/8), 895–909.
Scotese, C., L. Gahagan, and R. Larson (1988), Plate tectonic reconstructions of the Cretaceous and Cenozoic ocean basins, *Tectonophysics*, *155*, 27–48.
Seidl, M., and W. Dietrich (1992), The problem of channel erosion into bedrock, *Catena Supp.*, *23*, 101–124.
Séranne, M., and C.-R. Nzé Abeigne (1999), Oligocene to Holocene sediment drifts and bottom currents on the slope of Gabon continental margin (west Africa): Consequences for sedimentation and southeast Atlantic upwelling, *Sediment. Geol.*, *128*, 179–199.
Sestini, G. (1989), Nile Delta: A review of depositional environments and geological history, in *Deltas: Sites and Traps for Fossil Fuels*, edited by M. K. G. Whately and K. T. Pickering, pp. 99–127, Blackwell Scientific Publications, Oxford.

Sklar, L., and W. Dietrich (2001), Sediment and rock strength controls on river incision into bedrock, *Geology*, *29*(12), 1087–1090.
Smith, R., T. Mason, and J. Ward (1993), Flash-flood sediments and ichnofacies of the late Pleistocene Homeb Silts, Kuiseb River, Namibia, *Sediment. Geol.*, *85*, 579–599.
Swezey, C. (2009), Cenozoic stratigraphy of the Sahara, northern Africa, *J. Afr. Earth. Sci.*, *53*(3), 89–121.
Sykes, L. (1978), Intraplate seismicity, reactivation of preexisting zones of weakness, alkaline magmatism, and other tectonism postdating continental fragmentation, *Rev. Geophys.*, *16*(4), 621–688.
Tapley, B., et al. (2005), GGM02—An improved Earth gravity field model from GRACE, *J. Geod.*, *79*(8), 467–478.
Tarboton, D. (1997), A new method for the determination of flow directions and upslope areas in grid digital elevation models, *Water Resour. Res.*, *32*, 309–319.
Thorpe, R., and K. Smith (1974), Distribution of Cenozoic volcanism in Africa, *Earth Planet. Sci. Lett.*, *22*(1), 91–95.
Tinker, J., M. de Wit, and R. Brown (2008), Mesozoic exhumation of the Southern Cape, South Africa, quantified using apatite fission track thermochronology, *Tectonophysics*, *455*(1-4), 77–93.
Tokam, A.-P., C. Tabod, A. Nyblade, and J. Juli (2010), *Geophys. J. Int.*, *183*(2), 1061–1076, Structure of the crust beneath Cameroon, West Africa, from the joint inversion of Rayleigh wave group velocities and receiver functions, doi:10.1111/j.1365-246X.2010.04776.x.
Van der Beek, P., M. Summerfield, J. Braun, R. Brown, and A. Fleming (2002), Modeling postbreakup landscape development and denudational history across the southeast African (Drakensberg Escarpment) margin, *J. Geophys. Res.*, *107*(B12), 2351, doi:10.1029/2001JB000744.
Van der Wateren, F., and T. Dunai (2001), Late Neogene passive margin denudation history—Cosmogenic isotope measurements from the central Namib desert, *Global Planet. Change*, *30*, 271–307.
Veldkamp, A., E. Buis, J. Wijbrans, D. Olago, E. Boshoven, M. Marée, and R. van den Berg van Saparoea (2007), Late Cenozoic fluvial dynamics of the River Tana, Kenya, and uplift dominated record, *Quat. Sci. Rev.*, *26*(22-24), 2897–2912.
Walford, H. (2003), Spatial and temporal variation of African epeirogeny, PhD dissertation, Univ. of Cambridge.
Walford, H., N. White, and J. Sydow (2005), Solid sediment load history of the Zambezi delta, *Earth Planet. Sci. Lett.*, *238*(1-2), 49–63.
Whipple, K. (2001), Fluvial landscape response time: How plausible is steady-state denudation?, *Am. J. Sci.*, *301*, 313–325.
Whipple, K., and G. Tucker (1999), Dynamics of the stream-power river incision model: Implications for height limits of mountain ranges, landscape response timescales, and research needs, *J. Geophys. Res.*, *104*(B8), 17,661–17,674.
White, N., and B. Lovell (1997), Measuring the pulse of a plume with the sedimentary record, *Nature*, *387*, 888–891.
White, R., and D. McKenzie (1995), Mantle plumes and flood basalts, *J. Geophys. Res.*, *100*, 17,543–17,585.
Whittaker, A. (2012), How do landscapes record tectonics and climate?, *Lithosphere*, *4*(2), 160–164.
Wichura, H., R. Bousquet, R. Oberhänsli, M. Strecker, and M. Trauth (2010), Evidence for middle Miocene uplift of the East African Plateau, *Geology*, *38*(6), 543–546.
Wienecke, F., and U. Rust (1975), Zur relativen und absoluten Geochronologie der Reliefentwicklung an der Küste des mitteleren Südwestafrika, *Eiszeitalter und Gegenwart*, *26*, 241–250.
Winterbourne, J., A. Crosby, and N. White (2009), Depth, age and dynamic topography of oceanic lithosphere beneath the heavily sedimented Atlantic margin, *Earth Planet. Sci. Lett.*, *287*(1-2), 137–151.
Woolley, A. (2001), *Alkaline Rocks and Carbonatites of the World. Part 3: Africa, Geol. Soc. London*, 372 pp., Burlington, London.
Wu, S., R. Bras, and A. Barros (2006), Sensitivity of channel profiles to precipitation properties in mountain ranges, *J. Geophys. Res.*, *111*, F01024, doi:10.1029/2004JF000164.